J. Fluid Mech. (1993), *vol.* 254, *pp.* 437–466

Gas bubbles bursting at a free surface

By J. M. BOULTON-STONE AND J. R. BLAKE
School of Mathematics and Statistics, University of Birmingham, Edgbaston,
Birmingham B15 2TT, UK

(Received 19 October 1992 and in revised form 23 March 1993)

When a small air bubble bursts from an equilibrium position at an air/water interface, a complex motion ensues resulting in the production of a high-speed liquid jet. This free-surface motion following the burst is modelled numerically using a boundary integral method. Jet formation and liquid entrainment rates from jet breakup into drops are calculated and compared with existing experimental evidence. In order to investigate viscous effects, a boundary layer is included in the calculations by employing a time-stepping technique which allows the boundary mesh to remain orthogonal to the surface. This allows an approximation of the vorticity development in the region of boundary-layer separation during jet formation. Calculated values of pressure and energy dissipation rates in the fluid indicate a violent motion, particularly for smaller bubbles. This has important implications for the biological industry where animal cells in bioreactors have been found to be killed by the presence of small bubbles.

1. Background

1.1. *Introduction*

When a bubble bursts at a free surface, the surface tension rapidly pulls the rim where they intersect outward and downward. Eventually, a ring of fluid at the base of what was the bubble contracts to a point, throwing a plume of fluid upward in the form of a high-speed jet. The jet will often break up into a number of drops. The corresponding downward jet may be expected to advect vorticity from the separated boundary layer into the region beneath the bubble. Various aspects of this motion have been studied experimentally by a number of researchers – Kientzler *et al.* (1954), Newitt, Dombrowski & Knelman (1954), Garner, Ellis & Lacey (1954) and MacIntyre (1972). A numerical model based on an inviscid boundary integral scheme is used in this paper to model these bursting processes. Viscous effects are included in an attempt to model the boundary layer and subsequently the distribution of vorticity in the downward jet region.

1.2. *Motivation for the study*

Cells, cultivated in a bioreactor (figure 1), have been shown to be damaged by gas bubbles used to aerate the culture medium. Corresponding cell death rates are greatest (Handa 1986; Handa, Emery & Spier 1987) for many small bubbles rather than a few large ones. The fact that a significant proportion of cell damage occurs in a region near to the reactor free surface has been indicated by a number of experimenters (Kioukia 1990; Kunas & Papoutsakis 1990). It is also interesting to note that the ability of the reactor to produce a stable, slowly draining foam, when certain surface active chemicals are present, in particular Pluronic-F68 (a co-polymer of propylene oxide; produced by BASF, UK), greatly reduces the tendency for bubbles to damage cells.

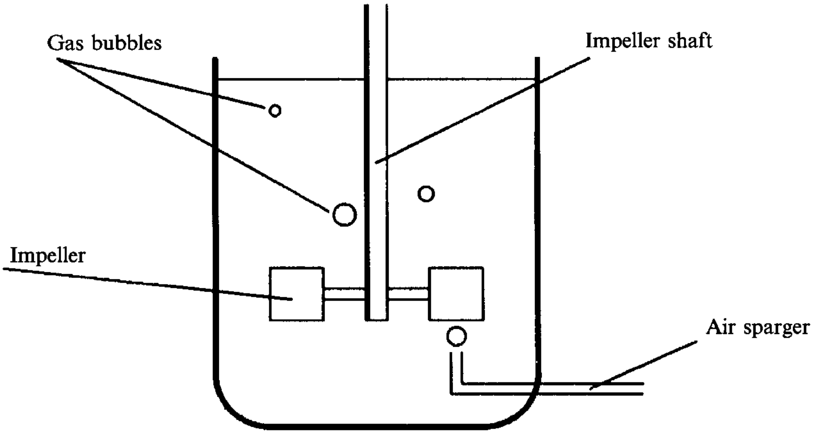

FIGURE 1. Components of a bioreactor, with the air sparger placed beneath the agitator.

Conversely, it has been demonstrated (Oh *et al.* 1989) that with purely surface aeration, cell death rates are largely independent of the agitation intensity used to evenly distribute nutrients through the reactor medium. All of this points to the possibility that bubble/free-surface interactions are somehow detrimental to cells.

The role of bubble interactions with the agitator impeller blade is another possible cause of damage. Recent experiments by Oh *et al.* (1992) suggest that cell damage is increased by positioning the air sparger beneath the impeller. The effects of this are however two-fold: it will increase the number of bubble/impeller interactions and it will also split large bubbles into smaller ones which are known to be more lethal at the free surface.

The bursting of bubbles at the free surface has become a prime suspect in the search for the cell damage mechanism, but it is apparent that there is no complete agreement as to the precise cause. In this paper, we seek to study physical aspects of the bursting of a bubble at a free surface as a contribution to this vital aspect of improving aeration in bioreactors to an extent where they become economically viable.

1.3. *Film rupture*

There is a substantial body of literature relating to films, and film drainage. The assumptions that must be made when dealing with thin films are completely different from those used below for a bubble in a high Reynolds number flow. Here, viscosity plays an important role in determining the drainage and stability properties of lamellae. There are three main reasons for film stability (see for example Bikerman 1973): surface viscosity, the Marangoni effect, and to a lesser extent electrostatic repulsion forces. In opposition to these electrostatic forces there are London–van der Waals forces that tend to pull the two sides of the film together, thus increasing the tendency to rupture. However the last two of these forces act over a very short range (of the order of 100 nm) and thus only have effect in the latter stages of thinning. Early on, while the film is thicker, there are two main mechanisms for drainage. Obviously, one is gravity. The second is due to Plateau borders (see Bikerman 1973). These are regions of high surface curvature, particularly in foams, causing low pressures at the 'corners' of a bubble. This mechanism is not so important when applied to a single bubble, where the curvature is almost constant before it bursts.

A film is said to be unstable (Scheludko 1962) if there is some critical thickness at which small perturbations on the surface will grow causing a hole to appear which, provided that it is big enough (Taylor & Michael 1973), then expands due to surface tension, thus rupturing the film.

With respect to bubbles approaching a free surface, experimental and theoretical aspects are considered in a number of papers. Allan, Charles & Mason (1961) measured the thickness of the film above a bubble. They found that the thinnest part of the film moves out from the centre to a circular rim. The radius of this rim, c, which remained almost constant, was found to agree well with the expression $c = (Eo/6)^{\frac{1}{2}}$, where Eo is the Eötvos number which is based on a balance of surface tension and buoyancy forces. The thinning rates found match theoretical estimates based on a pair of parallel disks or on the film between a rigid sphere and a free surface. They also observed that the presence of surfactants markedly reduced the thinning rates.

The effect of the approach speed of a bubble towards a free surface was investigated by Kirkpatrick & Lockett (1974). They found that for larger velocities (above about 1 cm/s for 2.5 mm radius bubbles in water) the thinning process does not have time to complete before the bubble is decelerated to rest by surface tension, which may then push it back into the fluid. In contrast, a bubble that is released just below the surface and so does not have time to accelerate to its terminal velocity is found to burst almost immediately, without bouncing. A simple mathematical model, based on the fact that the rate of thinning is inversely related to the area of the film was developed, leading to the same general conclusion. Minor impurities in the water were found to be insignificant, but with a larger amount of surfactant (0.6 M sodium chloride) the coalescence times became longer, with little difference between small and large approach velocities.

Hahn, Chen & Slattery (1985) used a lubrication theory approximation including the effects of London–van der Waals forces to model the draining of a film above a bubble. In this way they were able to obtain estimates for the rupture time, taken as the time for the rim thickness to become zero. However, they mentioned that the geometry used, which prevents any asymmetric instabilities, and the assumption that there is no tangential motion on the surfaces due to the presence of surfactants, means that the model gives only an upper bound for the rupture time. The effect of electrostatic repulsion was also neglected.

1.4. *Previous studies of bursting bubbles*

One of the earliest investigations of film rupturing was by Lord Rayleigh (1891), who applied high-speed photography to view the bursting of soap films. More up-to-date photographic studies have also been undertaken. Kientzler *et al.* (1954) show pictures of the breakup of the high-speed liquid jet that follows bubble burst. Newitt *et al.* (1954) showed that there are two types of drop released after the burst: large ones emanating from the jet mentioned above, but also smaller ones from the liquid film above the bubble. This thin lamella breaks up into a number of tiny droplets which are projected sideways by the expansion of the bursting film and upwards by the rush of gas as the pressure in the bubble is released.

In a more comprehensive study, MacIntyre (1972) showed that the film, as it breaks, 'rolls-up' into an expanding toroidal rim. This rim may break irregularly into a number of tiny droplets. He mentions that this rim of the film is expanding too rapidly to be broken up by capillary ripples, as in the case of the jet. Instead, this breakup is due to turbulence from the escaping air coupled with the effects of variations of surface tension and film thickness. After bubble burst, what remains of the toroidal rim follows a ripple down the sides of the bubble. By using dyes in the fluid, it was shown that the liquid in the jet originates in a thin layer surrounding the bubble crater. Very little mixing of the dye with surrounding fluid during jet formation indicated to MacIntyre that the flow at the base of the jet is irrotational. MacIntyre was also able to observe the corresponding downward jet of fluid that must occur on grounds of momentum conservation.

Evidence relating to the origin of the material in the jet is significant in the study of cell damage by bubbles, since it has been reported by Blanchard & Syzdek (1972) that bacteria tend to become adsorbed onto bubble surfaces. Similar results have been found for insect cells by Bavarian, Fan & Chalmers (1991). This was followed up by Chalmers & Bavarian (1991) who claimed that the hydrodynamic forces due to the shear in the boundary layer around the walls of the bubble cavity are sufficiently large to kill cells. They also postulated a second mechanism based on the small length of fluid that is accelerating as the bubble bursts (Culick 1960), that is that cells may be struck by the toroidal rim as they sit on a stationary part of the bursting lamella.

1.5. *Aims*

The primary aim of this study is to produce a numerical model of a bursting bubble, which agrees with the experimental results indicated above. In particular, the model should predict the high-speed liquid jet, together with the corresponding downward jet. Calculations can then be made as to the stresses imposed on a particle in the vicinity of the bursting bubble. The effects of viscosity, leading to a boundary layer and high shear rates, are also of interest as they may further increase the damaging potential of the bubble. An estimate of the contribution to the stress from vorticity in the region of the downward jet is sought. Such information may provide useful evidence for or against particular proposed cell damage mechanisms.

This paper does not address a numerical study of the film rupturing process itself, nor does it discuss further the stresses imposed on a particle resting on the film as it breaks: this will be left for the future. It is, however, important to consider the initial height of the bubble in the liquid in order to obtain a realistic figure for the energy released when it bursts.

2. Problem statement

2.1. *Inviscid formulation*

The photographic evidence of Kientzler *et al.* (1954) indicates that Reynolds numbers for a bubble bursting, from the time just after film rupture to the rise of the jet, are of the order of 1000. We may therefore assume that, up until the formation of the jet, any vorticity is limited to thin boundary layers around the air/water interfaces, so that the velocity distribution may be reasonably represented by potential flow, $\boldsymbol{u} = \nabla\phi$. The corresponding Reynolds numbers for bubbles rising under gravity are also large – of the order of 700 for bubbles as small as 0.1 cm radius moving at terminal velocity (see Levich 1962 or Clift, Grace & Weber 1978). We therefore assume that the inviscid model is also relevant for bubble rise. Since the density of the atmosphere and the gas contained in the bubbles is small compared with that of the liquid, atmospheric pressure and the gas pressures within each of the bubbles is assumed uniform. The relative volume change for a bubble containing an ideal gas at fixed temperature is given by

$$V/V_0 \approx (1-\rho g \Delta z/p_{atm})^{-1}. \tag{2.1}$$

If p_{atm} is atmospheric pressure and we assume that the total translation of the bubble, Δz, is only a few bubble radii, then $\rho g \Delta z/p_{atm} \ll 1$ and we may assume that the bubble volumes remain constant.

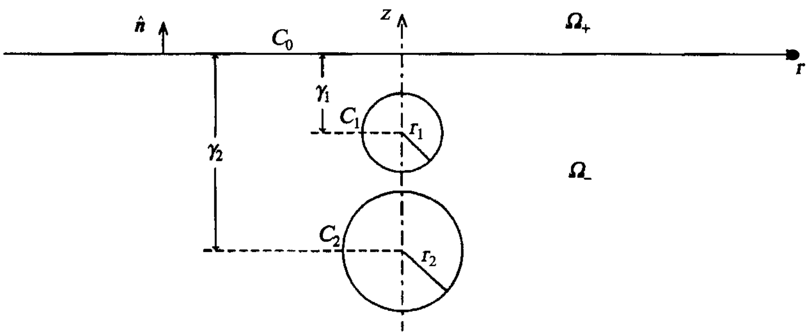

FIGURE 2. The initial position of bubbles C_1 and C_2 below the free surface, C_0. In most calculations presented, the free surface is not flat as depicted, but takes the shape of a bubble for which the film cap has just ruptured, together with a meniscus extending to infinity (see figure 3).

Although in the calculations shown below there is at most one bubble rising near a free surface together with one bubble in the process of bursting, it is more convenient to formulate the axisymmetric problem for M bubbles below a free surface. The solution domain, Ω_- (see figure 2), is defined to be the semi-infinite region bounded above by the free surface, C_0, and internally by each of the bubbles C_m, $(m = 1,\dots,M)$. The free surface coincides with the (x,y)-plane at infinity. Normals are taken as pointing outwards from Ω_-, into the gaseous phase.

Initially, bubbles are spherical with non-dimensional radii r_m, lengths being scaled with respect to the radius of bubble 1, which we denote by a. Bubble m is situated on the z-axis at a distance $\gamma_m(>0)$ below C_0. We further scale times with respect to $(\rho a^3/\sigma)^{\frac{1}{2}}$ and pressures by the factor σ/a, σ being the surface tension.

The code allows either bubbles to rise up to an initially flat free surface and burst as they reach it, or that a bubble will have just burst at $t = 0^-$, when the calculation is started. The latter option allows us to include more physical reality into the problem without worrying too much about surface drainage. The method for finding the initial surface shape in this case is discussed in §2.2.

In order to develop a numerical scheme for the associated moving boundary problem, two conditions are required at each boundary. The dynamic boundary condition, expressing the time dependence of the velocity field through the potential, comes from a consideration of the Bernoulli equation,

$$p_\infty = p+\tfrac{1}{2}|\boldsymbol{u}|^2+\frac{\partial\phi}{\partial t}+\tfrac{1}{4}Eo\, z, \tag{2.2}$$

evaluated at the interfaces. In (2.2), p_∞ is the fluid pressure at infinity, just below the free surface. The Eötvos number, $Eo = 4\rho g a^2/\sigma$, enters as a result of the pressure scaling (σ/a). It measures the bubble size and represents the square of the ratio of the timescale associated with the collapse, due to surface tension, of a spherical cavity whose contents remain fixed at the ambient pressure of the fluid and the timescale associated with the rise of a bubble due to gravity. During bubble burst, this parameter therefore measures the relative importance of bubble rise and bubble collapse. For the smallest bubbles, the effect of buoyancy will clearly be secondary to surface tension forces.

If viscous stresses in the thin boundary layers are ignored, a pressure balance may be used across each interface. The pressure just outside the surface C_m $(m = 0,\dots,M)$ is given by

$$p = p_m(t)-\kappa, \tag{2.3}$$

where κ is twice the mean curvature. Here, $p_m(t)\,(m = 1, \dots, M)$ is the pressure inside the mth bubble and $p_0(t) \equiv p_{atm}$ is the constant atmospheric pressure, which is also equal to p_∞ from (2.2) since the free surface is assumed flat at infinity.

Combining (2.2) and (2.3) evaluated at a general time and initially, and employing the substantial derivative in the form

$$\frac{\mathrm{D}\phi}{\mathrm{D}t} = \frac{\partial\phi}{\partial t} + |\boldsymbol{u}|^2, \tag{2.4}$$

gives an equation for the time evolution of the potential on C_m,

$$\left.\frac{\mathrm{D}\phi}{\mathrm{D}t}\right|_{C_m} = \tfrac{1}{2}|\boldsymbol{u}|^2 - \tfrac{1}{4}Eo(z+\gamma_m) + \kappa - \kappa_m + p_m(0) - p_m(t). \tag{2.5}$$

In (2.5), $\kappa_m(= 2/r_m)$ is the initial curvature for bubble m. Note that κ_0 and γ_0 are taken to be zero.

In order to eliminate the unknown pressure terms in (2.5) we introduce, in a similar manner to Lundgren & Mansour (1991), modified surface potentials defined by

$$f|_{C_m} = \phi|_{C_m} + k_m, \tag{2.6}$$

where
$$k_m(t) = \int_0^t (p_m(t') - p_m(0))\,\mathrm{d}t', \quad m = 0, \dots, M, \tag{2.7}$$

and we work with f rather than ϕ. With this definition, the dynamic condition (2.5) becomes

$$\left.\frac{\mathrm{D}f}{\mathrm{D}t}\right|_{C_m} = \tfrac{1}{2}|\boldsymbol{u}|^2 - \tfrac{1}{4}Eo(z+\gamma_m) + \kappa - \kappa_m, \quad m = 0, \dots, M. \tag{2.8}$$

Writing the dynamic boundary condition (2.8) in terms of the initial bubble depth and curvature, rather than including these constants in the unknown k_m, ensures that changes of f for each bubble will be initially centred on zero, thus reducing round-off errors, especially for deeply submerged or very small bubbles.

The surface C_m is represented parametrically by the function $\boldsymbol{q}_m(s, \theta, t)\,(0 \leqslant s \leqslant l_m$, $m = 0, \dots, M)$ where s is an arclength parameter and θ is an azimuthal angle. For bubbles, l_m is the total arclength around B_m, the intersection of C_m with the half-plane $\theta = 0$, and $l_0 \equiv \infty$. The kinematic condition expresses the assumption that there is no mass transfer across interfaces, and thus a particle that lies on a surface will remain there and move with its local velocity, namely

$$\frac{\partial \boldsymbol{q}_m}{\partial t}(s, \theta, t) = \nabla\phi(\boldsymbol{q}_m(s, \theta, t), t), \quad m = 0, \dots, M. \tag{2.9}$$

To keep the bubble volumes constant, constraint equations in the form of the line integrals

$$\int_{B_m} \frac{\partial\phi}{\partial n} r(s)\,\mathrm{d}s = 0, \quad m = 1, \dots, M \tag{2.10}$$

are used, where $r(s)$ is the distance of a point from the axis of symmetry.

2.2. *Bursting the bubbles*

Certain questions have to be addressed in order to produce a good model of the bursting process. As the film above the bubble will be very thin when it ruptures, between about 10 nm at its thinnest parts (Vrij 1966) and a few microns elsewhere, we assume for the purposes of this paper that the film itself will have no significant effect on the subsequent motion. The rupture of the film may have dire consequences for cells adsorbed onto the upper surface of the bubble, but this is neglected in this investigation.

If we can ignore the film, then when a bubble is 'burst' numerically, a decision still has to be made as to the amount of film above the bubble to remove before reconnecting the bubble cavity to the free surface. This will invariably be greater than the total amount of fluid in an actual film because of the difficulty in calculating the bubble and surface motion with the bubble much closer to the surface than the length of a single boundary integral element (see §3). However, numerical experimentation has shown that, provided not too much fluid above the bubble is thrown away, this has little effect on the subsequent bursting motion. It would, in any case, be inappropriate to assume that the irrotational model could accurately predict the fluid flow in the film itself when it becomes even moderately thin: the thinning rate would be too rapid. In the case where surfactants are present various physico-chemical phenomena such as surface viscosity may become important so that even stress-free interfacial boundary conditions become invalid. It is thus hard to see how the rupture time can be determined based on the calculated thickness of the film other than by matching a modified lubrication layer for the film on to the inviscid model. The rupture-time calculations of Hahn *et al.* (1985) are likewise difficult to implement, firstly because they are inaccurate, as indicated in § 1.3, but also because of the problem of identifying with any certainty their initial time, when the draining rate of the film above the bubble is independent of radial position. It is suggested, however, that this time will be close to the time that the bubble comes to rest at the surface.

It seems clear that one of the most important factors determining the motion following film rupture, in terms of the energy released, is the height of the top of the bubble above the equilibrium free-surface position. The experimental study of Kirkpatrick & Lockett (1974) indicates that bubbles moving at speeds approaching terminal velocity, upon reaching the free surface tend to come to rest and bounce a couple of times before bursting. It has also been observed (see for example Newitt *et al.* 1954 or Allan *et al.* 1961) that a bubble may rest for a short time at the free surface before bursting. In any case, we assume that the thinning of the film and the instabilities which eventually rupture it when it reaches a critical thickness are to some extent asynchronous with the bouncing of the bubble and that, on average, a bubble will burst at its static equilibrium position when the buoyancy force is equal to the downward component of surface tension. For a spherical bubble in a pure liquid, the non-dimensional height above the surface of the top of the bubble would be approximately

$$h = 1-(1-Eo/6)^{\frac{1}{2}}. \tag{2.11}$$

This is equivalent to the formula given by Allan *et al.* (1961) for the radius of the rim of intersection of the free surface and the bubble, in terms of the bubble radius. Here, we use a pressure balance to find the equilibrium bubble and meniscus shapes, employing (2.11) as a first approximation. If σ_{ij} are the surface tensions of the interfaces (i,j) (see figure 3) then force balances in the r- and z-directions give us respectively

$$\sigma_{13}\cos\theta_c = \sigma_{12}\cos\phi_c + \sigma_{23}\cos\psi_c - K/r_c \tag{2.12}$$

and

$$\sigma_{13}\sin\theta_c = \sigma_{12}\sin\phi_c + \sigma_{23}\sin\psi_c, \tag{2.13}$$

where K is the line tension from the intersection of the three interfaces. A subscript c denotes evaluation at this contact line. In general, the value of K depends on the

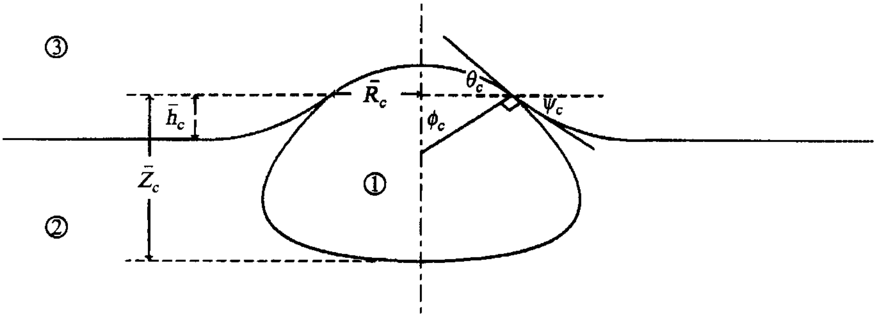

FIGURE 3. Schematic diagram of a bubble at a free surface in the initial static equilibrium position just prior to film rupture.

geometric configuration of the interfaces as well as the physical properties of the fluids (see Ivanov, Kralchevsky & Nikolov 1986).

It is convenient at this point to follow Ivanov *et al.* (1986) and rescale lengths with respect to the mean radius of curvature, b, of the lowest point of the bubble. Correspondingly scaled quantities will be indicated by an overbar. We also introduce the quantity $\beta = \rho g b^2/\sigma$ (similar to the Eötvos number Eo), where $\sigma = \sigma_{12} = \sigma_{23}$. If we write $\bar{\tau} = \sigma_{13}/\sigma$ and $\bar{K} = K/b\sigma$, the experimental evidence of Ivanov *et al.* (1986) suggests that

$$|\bar{\tau}-2| \ll 1 \quad \text{and} \quad |\bar{K}| \ll 1. \tag{2.14}$$

As angles θ_c, ϕ_c and ψ_c must be acute, (2.12) and (2.13) give approximate solutions $\theta_c = \frac{1}{2}(\phi_c+\psi_c)$ and $\phi_c = \psi_c$, namely $\theta_c = \phi_c = \psi_c$.

Let $(\bar{R}, \bar{Z})$ be the rectangular coordinates of a point in a half-plane containing the axis of symmetry, centred on the lowest point of the bubble crater. A simple consideration of the pressure jump across the interface (1, 2) shows that the shape of the bubble cavity is described by the differential system

$$\frac{\mathrm{d}\bar{R}}{\mathrm{d}\phi} = \frac{\bar{R}\cos\phi}{(2+\beta\bar{Z})\bar{R}-\sin\phi}, \tag{2.15}$$

$$\frac{\mathrm{d}\bar{Z}}{\mathrm{d}\phi} = -\tan\phi\frac{\mathrm{d}\bar{R}}{\mathrm{d}\phi}, \tag{2.16}$$

with boundary conditions

$$\bar{R} = \bar{Z} = 0 \quad \text{at} \quad \phi = \pi. \tag{2.17}$$

We denote the values of $\bar{R}$ and $\bar{Z}$ at $\phi = \phi_c$ by $\bar{Z}_c$ and $\bar{R}_c$ respectively.

Similarly, the meniscus (interface (2.3)) has shape $\bar{z} = \bar{h}(\bar{r})$ which is governed by the second-order equation

$$\bar{h}'' = (-\bar{h}'/r+\beta\bar{h}(1+\bar{h}'^2)^{\frac{1}{2}})(1+\bar{h}'^2), \tag{2.18}$$

with the two-point boundary conditions

$$\bar{h}'(\bar{R}_c) = -\tan\psi_c \quad \text{and} \quad \bar{h}(\infty) = 0. \tag{2.19}$$

Asymptotic solutions for both the bubble cavity and meniscus shapes exist for small values of β and $\bar{R}_c$ respectively (see Ivanov *et al.* 1986 and Lo 1983). However, for larger bubbles these expressions are less accurate and so a numerical solution is used here.

The system given by (2.18) and (2.19) can be solved using a technique similar to that of Princen (1963), by choosing a value for $\bar{h}_c \equiv \bar{h}(\bar{R}_c)$ and performing a simple bisection search depending on whether the solution tends to infinity or dips below the $z = 0$ plane. Since the meniscus meets the bubble at $\bar{r} = \bar{R}_c$, we have that the bubble position in the fluid is given by

$$\bar{z} = \bar{Z}(\phi) + \bar{h}_c - \bar{Z}_c. \tag{2.20}$$

We further assume the film separating the bubble from the atmosphere to the very thin and thus gravity forces negligible compared to the effect of pressure so that the film may be taken to be spherical with radius $\bar{c}$. Using this to equate the pressure in the bubble given by the jump across the spherical film with that given by the hydrostatic pressure at the bottom plus the corresponding jump due to surface tension there gives

$$4/\bar{c} = 2 + \beta(\bar{Z}_c - \bar{h}_c). \tag{2.21}$$

Since the dome is spherical, $\bar{R}_c = \bar{c} \sin \theta_c$ and (2.21) can be written as

$$\bar{R}_c(1 + \tfrac{1}{2}\beta(\bar{Z}_c - \bar{h}_c)) = 2 \sin \phi_c. \tag{2.22}$$

Equation (2.22) fixes the height of the bubble in the fluid, but we also need an equation to set the volume. The volume of the bubble with the new scalings is

$$\bar{V} = \tfrac{4}{3}\pi(Eo/4\beta)^{\frac{3}{2}}. \tag{2.23}$$

Note that the volume, $\bar{V}$, is calculated by adding the volume for the region of the bubble below the ring of intersection, $\bar{V}_{12}$, which can be found numerically, to the volume of the spherical dome with radius given by (2.21), thus

$$\bar{V} = \bar{V}_{12} + \pi[\tfrac{2}{3}(\bar{c}^3 - (\bar{c}^2 - \bar{R}_c^2)^{\frac{3}{2}}) - \bar{R}_c^2(\bar{c}^2 - \bar{R}_c^2)^{\frac{1}{2}}]. \tag{2.24}$$

The solution method is to firstly select an approximation for the unknown variables, ϕ_c and β. These are given by the assumption that the bubble is almost spherical, of radius a with the top a non-dimensional height given by (2.11) above the free surface, so that

$$\bar{R}_c^{(0)} = (Eo/6)^{\frac{1}{2}}, \tag{2.25}$$

thus

$$\phi_c^{(0)} = \arcsin(\bar{R}_c^{(0)}), \tag{2.26}$$

and

$$\beta^{(0)} = \tfrac{1}{4}Eo. \tag{2.27}$$

For this initial approximation, we must restrict Eo to be less than 6, which imposes a maximum on the bubble radius of about 0.34 cm. Newton iteration is then used to calculate the values of ϕ_c and β subject to (2.22) and (2.23), with $\bar{V}$ given by (2.24).

An alternative bursting mechanism which will work well only for small bubbles, but that illustrates the importance of a physically realistic bursting procedure for larger bubbles can be used for bubbles that have been followed numerically from a distance below the free surface. This is to simply burst the bubble when its uppermost nodes become closer to the free surface than some critical distance. Any points on the bursting bubble or free surface closer together than some other prescribed distance are removed. The remains of the bubble and free surface are then rejoined to form an indented free surface. We assume that the burst takes place in an instant, so that the potentials on the other parts of the bubble are unaffected. Note, however, that when the mth bubble bursts, the constant k_m must be subtracted from the potentials on that bubble before reconnecting it to the free surface. To smooth the new surface slightly at the point of joining, a new node is added at the midpoint of the first nodes removed from the old surfaces, and the potential at this node is simply taken as the average of the potentials at the old two nodes. The calculation is then allowed to continue. This method of bursting can be anticipated to result in a significant overestimate of the energy release when a large bubble bursts, as shown below.

3. Solution by the boundary integral method

The solution method relies on writing Laplace's equation for the potential, ϕ, in the form of an integral equation, which can be solved in a discrete form. Define the surfaces $\partial\Omega$, the boundary of Ω_-, and $C = C_0(R) \cup \tilde{C}_0(R) \cup C_1 \cup \cdots \cup C_M$, where $\tilde{C}_0(R)$ is a spherical arc of radius R, centred at a point $x^* \in \Omega_- \backslash \partial\Omega$, and take $C_0(R)$ to be the finite portion of C_0 extending as far as $\tilde{C}_0(R)$, in such a way that $\tilde{C}_0(R) \cup C_0(R)$ encloses all of the C_m ($m = 1, \ldots, M$). If we now chose a point x on $\partial\Omega$, we may use Green's integral formula written in the form

$$\phi(x^*) - \phi(x) = \int_C \left(G(x^*, x') \frac{\partial\phi}{\partial n}(x') - (\phi(x') - \phi(x)) \frac{\partial G}{\partial n'}(x^*, x') \right) \mathrm{d}S', \tag{3.1}$$

where

$$G(x^*, x') = \frac{1}{4\pi|x^* - x'|} \tag{3.2}$$

is the fundamental solution of the three-dimensional Laplace equation. As the fluid is at rest at infinity, we assert that $\phi(x) \to 0$ as $|x| \to \infty$ and so for $x' \in \tilde{C}_0(R)$, $\mathrm{d}S = O(R^2)$, $\phi = O(1/R)$ and $\partial\phi/\partial n = O(1/R^2)$ as $R \to \infty$. It is clear that the integral over $\tilde{C}_0(R)$ (with the exception of the term in $\phi(x)$ which approaches the value $-\frac{1}{2}\phi(x)$) behaves as $1/R$ and so vanishes when we take the limit $R \to \infty$. We also take the limit $x^* \to x$, which is trivially done, owing to the regularity of the integral. As the Cauchy principal value integral of the remaining term in $\phi(x)$ is now zero,

$$\tfrac{1}{2}\phi(x) = \int_{\partial\Omega} \left(G(x, x') \frac{\partial\phi}{\partial n}(x') - \phi(x') \frac{\partial G}{\partial n'}(x, x') \right) \mathrm{d}S', \quad x \in \partial\Omega. \tag{3.3}$$

Finally, substituting f for ϕ as in (2.6) and using the fact that $k_0(t) \equiv 0$, gives the expression

$$\tfrac{1}{2}f(x) = k_m + \int_{\partial\Omega} \left(G(x, x') \frac{\partial\phi}{\partial n}(x') - f(x') \frac{\partial G}{\partial n'}(x, x') \right) \mathrm{d}S', \quad x \in C_m, \quad m = 0, \ldots, M. \tag{3.4}$$

(The same formula can be derived for the case when C_0 is absent from $\partial\Omega$, that is the bubbles reside in an infinite fluid.)

The integral equation (3.4) is in a form suitable for use in the program described below which is a modified version of the code of Best & Kucera (1992), which was originally designed for cavitation and explosion bubbles in an infinite fluid.

The boundary of the solution domain is now discretized. Nodes, denoted by the position vectors p_{mi} where ($i = 0, \ldots, N_m$ and $m = 0, \ldots, M$), are distributed on the bounding arcs of the surfaces, B_m. In the Cartesian half-plane $\theta = 0$ these nodes have the coordinates (r_{mi}, z_{mi}).

For bubbles, nodes 0 and N_m lie on the central axis at the bottom and top respectively. Initially, nodes are equally spaced by arclength on the bubbles, and on the free surface they are placed on the portion $0 \leqslant r \leqslant R_{max}$ of B_0, for some large R_{max}, with the nonlinear distribtuion

$$r_{0i} = \frac{iR_{max}}{2N_0}(1 + (i - N_0 - 1)^{-2}), \quad i = 0, \ldots, N_0, \tag{3.5}$$

so that points are distributed more densely near the axis, where resolution is particularly important. Subsequently, R_{max} is allowed to alter dynamically with the position of the end node on the free surface, namely $R_{max}(t) = r_{0N_0}$. Similarly we define $Z_{max}(t) = z_{0N_0}$ and $F_{max}(t) = f_{0N_0}$. In order to evaluate the integral over the infinite free surface, an approximate expression is required for the quantities in the integrand of (3.4). The motion of a bursting bubble may be thought of as a superposition of harmonic modes of which the spherically symmetric mode, corresponding to the isotropic collapse of a cavity due to surface tension, may be represented by a potential sink. A consideration of the linearized boundary conditions for large r indicates that at $z = 0$, $\partial^2\phi/\partial t^2 \sim -\partial\phi/\partial z$. This condition is not satisfied by the sink alone but is satisfied by an image system that falls off as r^{-3}. The assumption of a dipolar far field is also consistent with the fully nonlinear boundary conditions and implies that the free-surface elevation is also of order r^{-3} for large r. Thus for the purposes of the numerical computations, we assume for $r > R_{max}$

$$f_0(r) \sim F_{max}(R_{max}/r)^3 \quad \text{and} \quad z_0(r) \sim Z_{max}(R_{max}/r)^3 \quad \text{as} \quad r \rightarrow \infty. \tag{3.6}$$

A similar asymptotic technique was used in the boundary integral method of Oguz & Prosperetti (1989), to calculate the motion of the contact line between a drop and a free surface.

Cubic splines are used to interpolate the surface nodes. The end conditions, dictated by symmetry, are that $\partial z_m/\partial s = 0$, $\partial f_m/\partial s = 0$ on the axis. Since the spline for the free surface only reaches as far as $r = R_{max}$, the conditions there are

$$\frac{\partial z_0}{\partial s} = \frac{-3z/r}{(1+(3z/r)^2)^{\frac{1}{2}}}, \quad \frac{\partial r_0}{\partial s} = (1+(3z/r)^2)^{-\frac{1}{2}} \quad \text{and} \quad \frac{\partial f_0}{\partial s} = \frac{-3f/r}{(1+(3z/r)^2)^{\frac{1}{2}}}, \tag{3.7}$$

thus ensuring continuity of first derivative with the analytic portion of the free surface. The asymptotic form for the normal derivative of the potential ψ, for large r, on the free surface is

$$\psi_0(r) \sim \Psi_{max}(R_{max}/r)^3 \quad \text{as} \quad r \rightarrow \infty, \tag{3.8}$$

where $\Psi_{max} = \psi_{0N_p}$.

The azimuthal integrations in (3.4) can be calculated analytically in terms of complete elliptic integrals (see for example Guerri, Lucca & Prosperetti 1981 or Taib 1985). The arclength integrations are then evaluated using an appropriate Gauss quadrature scheme, to yield a system of linear algebraic equations for the unknown normal derivatives, ψ_{mi}. Coupled with (3.4), the M equations of (2.10) allow calculation of the M constants, k_m.

4. Viscous effects

4.1. *Boundary-layer approximation*

As mentioned in §1, it has been proposed that a possible cause of cell damage is high shear stresses in the boundary layer of a bursting bubble. Independent calculations by J. J. Chalmers (1992, personal communication) suggest that the shear stresses occurring in the downward jet, particularly for small bubbles, may be large enough to cause cell damage. It is therefore of interest to calculate the vorticity development in the downward jet region. It is also important to gain information as to the effect of viscosity on the interface motion, particularly on the development of the jet where high rates of strain are expected.

There have been a number of studies where weak viscous effects have been included in otherwise inviscid boundary integral formulations. Miksis, Vanden-Broek & Keller (1982) included a modified boundary condition in calculations of the steady-state shape of a rising bubble. Their modification took into account only the change in the normal stress at the surface due to viscosity, and ignored the pressure drop across the boundary layer itself which, as they noted, becomes particularly important on the lower part of the bubble.

This was taken a stage further by Lundgren & Mansour (1988), where an analysis of the boundary-layer equations resulted in expressions for the pressure difference and normal component of the velocity perturbation due to the viscous layer. For completeness, we given an indication of the method of Lundgren & Mansour and then describe a way in which this can be extended so that the tangential component of the boundary-layer velocity can be obtained. With this information it is possible to identify approximate initial conditions for the vorticity distribution as the jet is about to form and thus gain some understanding of the flow in the downward jet.

Lundgren & Mansour's method (referred to as LM) is as follows. The velocity field is written in the form $\boldsymbol{v} = \boldsymbol{u} + \boldsymbol{U}$, where $\boldsymbol{u} = \nabla\phi$ is the usual potential flow field and $\boldsymbol{U} = \nabla \times \boldsymbol{A}$ is the rotational flow. For uniqueness, $\boldsymbol{A}$ is taken to be zero outside the boundary layer. Since the flow is axisymmetric, $\boldsymbol{A} = A\hat{\boldsymbol{\theta}}$. Likewise, the total pressure may be written as $p^* = p + P$, where P is the perturbation in pressure due to the boundary layer. The viscous boundary conditions are the usual ones for a free surface. Firstly, a balance of normal stress on either side of all interfaces is required:

$$-p_m(t) + \kappa = -p^* + 2Re^{-1}\hat{\boldsymbol{n}}\cdot\nabla\boldsymbol{v}\cdot\hat{\boldsymbol{n}}, \quad m = 0, \dots, M. \tag{4.1}$$

Secondly, due to the relatively low dynamic viscosity of the air, there should be no tangential stress at the surfaces:

$$\hat{\boldsymbol{t}}\cdot\nabla\boldsymbol{v}\cdot\hat{\boldsymbol{n}} + \hat{\boldsymbol{n}}\cdot\nabla\boldsymbol{v}\cdot\hat{\boldsymbol{t}} = 0. \tag{4.2}$$

Here, $\hat{\boldsymbol{t}}$ and $\hat{\boldsymbol{n}}$ are the tangent and normal to the generator of the axisymmetric bubble. The Reynolds number, Re, is given by $(\sigma a/\rho\nu^2)^{\frac{1}{2}}$.

On assuming that the bounday layer is thin, with thickness δ, and that the variation along a surface is of order unity, LM use the zero tangential stress condition (4.2) to make the approximation

$$\partial U_t/\partial n = -2\hat{\boldsymbol{t}}\cdot\nabla\boldsymbol{u}\cdot\hat{\boldsymbol{n}} + O(\delta^2), \tag{4.3}$$

which shows that $U_t = O(\delta)$ with $A = O(\delta^2)$ and from mass conservation $U_n = O(\delta^2)$. Here, subscripts n and t refer to normal and tangential components of a local curvilinear coordinate system fitted to the instantaneous interface shape. A consideration of the normal and tangential components of the Navier–Stokes equations shows that for viscous terms to be retained, the boundary-layer thickness must be related to the Reynolds number by $\delta = Re^{-\frac{1}{2}}$. Upon neglecting variations of P along the boundary layer, LM are able to integrate the tangential equation across it and produce an equation for the development of A at the surface. Likewise the normal equation is integrated across the boundary layer to give an expression for P at a surface, in terms of A and the irrotational velocity, $\boldsymbol{u}$. Before giving these expressions it is convenient, for brevity, to introduce the notation

$$\frac{\mathrm{D}\{\boldsymbol{w}\}h}{\mathrm{D}t} \equiv \frac{\partial h}{\partial t} + \boldsymbol{w}\cdot\nabla h. \tag{4.4}$$

This is a generalization of the usual material derivative, where the rate of change of a function of the flow field is taken following points that move with a velocity $\boldsymbol{w}$. This notation will prove useful when we consider the calculation of the tangential velocity due to the boundary layer, but is also appropriate here. The final boundary conditions found by LM give, in the context of the bubble bursting problem,

$$\frac{\mathrm{D}\{\boldsymbol{u} + U_n\hat{\boldsymbol{n}}\}A}{\mathrm{D}t} = -A\left(2\frac{\partial u_t}{\partial s} - 2\kappa^{(t)}u_n + \frac{\boldsymbol{u}\cdot\hat{\boldsymbol{r}}}{r}\right) + 2Re^{-1}\left(\frac{\partial u_n}{\partial s} + \kappa^{(t)}u_t\right) + O(\delta^3), \tag{4.5}$$

where $U_n = (\partial(rA)/\partial s)/r$ and $\kappa^{(t)}$ is the curvature of the interface in a plane through the axis of symmetry. Also

$$\frac{\mathrm{D}\{\boldsymbol{u}+U_n\hat{\boldsymbol{n}}\}\phi}{\mathrm{D}t} = \tfrac{1}{2}|(\boldsymbol{u}+U_n\hat{\boldsymbol{n}})|^2 + p_m(0) - p_m(t) - \tfrac{1}{4}Eo(z+\gamma_m) + \kappa - \kappa_m + 2A\left(\frac{\partial u_n}{\partial s} + \kappa^{(t)}u_t\right) + 2Re^{-1}\left(\frac{\partial u_t}{\partial s} - \kappa^{(t)}u_n + \frac{\boldsymbol{u}\cdot\hat{\boldsymbol{r}}}{r}\right) + O(\delta^3). \quad (4.6)$$

The modification to the pressure is likewise given by

$$P = 2A\hat{\boldsymbol{t}}\cdot\nabla\boldsymbol{u}\cdot\hat{\boldsymbol{n}} + O(\delta^3). \quad (4.7)$$

The model of LM is insufficient if we wish to go on to approximate the flow field after the boundary layer separates from the bubble cavity as the jet is about to form, since it does not include a scheme for calculating the total tangential velocities in the layer: the contribution to the tangential velocities is an order of magnitude higher than that for the normal velocities in the boundary layer. To do this, we solve a partial differential equation based on the tangential component of the boundary layer equation (LM's equation (4.18) with a total Lagrangian derivative),

$$\frac{\mathrm{d}U_t}{\mathrm{d}t} + U_t\hat{\boldsymbol{t}}\cdot\nabla\boldsymbol{u}\cdot\hat{\boldsymbol{t}} = Re^{-1}\frac{\partial^2 U_t}{\partial n^2} + O(\delta^2), \quad (4.8)$$

subject to the boundary conditions (4.3) at the surface and $U_t \rightarrow 0$ outside the thin boundary layer.

Equation (4.8) can be solved using a finite-difference scheme, by fitting a grid of points to the boundary-layer region. If we wish to continue to use the model of LM and the boundary integral scheme, it is possible to use (4.8) as an equation for the Lagrangian evolution of particles moving through the fluid in the viscous layer. As the problem is inherently unsteady, these grid points will move in relation to one another and thus it will be difficult to keep track of which nodes are closest to each other for the purpose of calculating derivatives. (For a review of techniques for following closest nodes in such problems see for example Boris 1989.) Alternatively, a scheme could be devised whereby points are remeshed after each time step to keep them on a more convenient grid. However a technique is used here in which the need to reposition at each time step is removed, except when the usual repositioning of surface nodes is performed in the boundary integral scheme. The idea uses the fact that the bubble or free surface is a stress-free interface, and consequently a material line that is normal to a surface will remain, locally, orthogonal – see the Appendix. Since this orthogonality is only local to the point on the surface, we 'linearize' the Lagrangian time derivative by writing

$$\frac{\mathrm{d}}{\mathrm{d}t} = \frac{\mathrm{D}\{\boldsymbol{v}\}}{\mathrm{D}t} = \frac{\mathrm{D}\{\boldsymbol{v}_0 - \eta(\hat{\boldsymbol{n}}\cdot\nabla\boldsymbol{v})|_0\}}{\mathrm{D}t} + (\boldsymbol{v} - \boldsymbol{v}_0 + \eta(\hat{\boldsymbol{n}}\cdot\nabla\boldsymbol{v})|_0)\cdot\nabla, \quad (4.9)$$

where η is the normal distance from a point to the surface and the subscript 0 denotes evaluation at the surface. It is clear from (4.9) that as $\eta \rightarrow 0$ the approximate Lagrangian derivative – following points moving at velocities $\boldsymbol{v}^* \equiv \boldsymbol{v}_0 - \eta(\hat{\boldsymbol{n}}\cdot\nabla\boldsymbol{v})|_0$ – becomes exact. Writing (4.8) in terms of this derivative gives us

$$\frac{\mathrm{D}\{\boldsymbol{v}^*\}U_t}{\mathrm{D}t} = Re^{-1}\frac{\partial^2 U_t}{\partial n^2} - U_t\hat{\boldsymbol{t}}\cdot\nabla\boldsymbol{u}\cdot\hat{\boldsymbol{t}} - (\boldsymbol{v} - \boldsymbol{v}_0 + \eta(\hat{\boldsymbol{n}}\cdot\nabla\boldsymbol{v})|_0)\cdot\nabla U_t + O(\delta^2). \quad (4.10)$$

The virtue of this approach is that if we follow mesh points which move with velocities given by $\boldsymbol{v}^*$, then as this is the exact Lagrangian derivative at the surface where the zero tangential stress condition (4.2) is applicable, the mesh lines normal to the surface will remain normal at the surface. The linearization further ensures that these lines remain straight since the transformation mapping the line to its new position a short time later is linear (as $\hat{\boldsymbol{n}}\cdot\nabla\boldsymbol{v}^* = (\hat{\boldsymbol{n}}\cdot\nabla\boldsymbol{v})|_0$). The advantages over more usual Lagrangian finite-difference schemes are that normal derivatives are always simple to evaluate; there is no need to store the position of the mesh points, only their distances from the surface; and, as mentioned above, there is no need to reposition the points other than occasionally as dictated by the underlying boundary integral scheme – see §4.2.

The new term on the right-hand side of (4.10) as compared with (4.8) can be shown to be of order δ^2 in the boundary layer. As we can assume that the potential flow field changes slowly in the boundary layer we can view the potential flow part of $\boldsymbol{v}^*$ as the error in the Taylor expansion of $\boldsymbol{u}$, and so if $\eta = O(\delta)$,

$$(\boldsymbol{v}-\boldsymbol{v}_0+\eta(\hat{\boldsymbol{n}}\cdot\nabla\boldsymbol{v})|_0)\cdot\nabla U_t = (\boldsymbol{U}-\boldsymbol{U}_0+\eta(\hat{\boldsymbol{n}}\cdot\nabla\boldsymbol{U})|_0)\cdot\nabla U_t+O(\delta^2). \tag{4.11}$$

Splitting the remaining velocities into their normal and tangential components shows the first two terms to be of order δ^2, leaving

$$\eta\left(\left.\frac{\partial U_t}{\partial n}\right|_0\hat{\boldsymbol{t}}+\left.\frac{\partial U_n}{\partial n}\right|_0\hat{\boldsymbol{n}}\right)\cdot\nabla U_t+O(\delta^2). \tag{4.12}$$

This is of order $\eta\delta$, which is of order δ^2 in the boundary layer. Knowing U_t to order δ is consistent with calculating A to order δ^2 since $U_t \approx \partial A/\partial n$.

The second term on the right-hand side of (4.10) can also be approximated. Expanding in a Taylor series,

$$\hat{\boldsymbol{t}}\cdot\nabla\boldsymbol{u}\cdot\hat{\boldsymbol{t}} = (\hat{\boldsymbol{t}}\cdot\nabla\boldsymbol{u}\cdot\hat{\boldsymbol{t}})|_0-\eta[\hat{\boldsymbol{n}}\cdot\nabla(\hat{\boldsymbol{t}}\cdot\nabla\boldsymbol{u}\cdot\hat{\boldsymbol{t}})]|_0+O(\eta^2). \tag{4.13}$$

Since this term is multiplied by U_t, the first-order correction in (4.13) may be ignored in the boundary layer. The final form of (4.10) is thus

$$\frac{\mathrm{D}\{\boldsymbol{v}^*\}U_t}{\mathrm{D}t} = Re^{-1}\frac{\partial^2 U_t}{\partial n^2}-U_t(\hat{\boldsymbol{t}}\cdot\nabla\boldsymbol{u}\cdot\hat{\boldsymbol{t}})|_0+O(\delta^2). \tag{4.14}$$

Derivatives of U_t are calculated by fitting quadratics to nodal values along a normal to the surface, with the value on the surface given by (4.3) and U_t assumed zero outside the boundary layer. This is then repeated to give the second derivatives.

The rate of change of the distance between the surface node and a corresponding mesh node on the normal to the surface is given by the difference in normal velocity between the surface and the mesh point. Thus if we now view η as a parametrization of a mesh normal to a surface with the linearized time derivative we see that

$$\partial\eta/\partial t = \eta(\hat{\boldsymbol{n}}\cdot\nabla\boldsymbol{v})|_0\cdot\hat{\boldsymbol{n}}. \tag{4.15}$$

Writing the continuity equation for the potential flow in terms of normal and tangential derivatives gives

$$\frac{\partial u_n}{\partial n}+\frac{\partial u_t}{\partial s}-\kappa^{(t)}u_n+\frac{\boldsymbol{u}\cdot\hat{\boldsymbol{r}}}{r} = 0, \tag{4.16}$$

so that (4.15) may be written as

$$\frac{\partial\eta}{\partial t} = -\eta\left.\left(\frac{\partial u_t}{\partial s}-\kappa^{(t)}u_n+\frac{\boldsymbol{u}\cdot\hat{\boldsymbol{r}}}{r}\right)\right|_0+O(\delta^2). \tag{4.17}$$

Note that as the linearized derivative matches with the total derivative at the boundary, the evolution of A and of ϕ can be approximated by using (4.5) and (4.6), however (4.6) first needs modifying to take account of the tangential component of the derivative by adding a term $U_t \hat{\boldsymbol{t}}\cdot\nabla\phi$ to both sides. This order-δ term simply corrects for the additional tangential motion without otherwise affecting the potential distribution on the surface. We write (4.6) as

$$\frac{\mathrm{D}\{\boldsymbol{v}_0\}\,\phi}{\mathrm{D}t} = \tfrac{1}{2}(|\boldsymbol{v}_0|^2 - U_t^2) + p_m(0) - p_m(t) - \tfrac{1}{4}Eo(z+\gamma_m) + \kappa - \kappa_m$$
$$+2A\left(\frac{\partial u_n}{\partial s} + \kappa^{(t)} u_t\right) + 2Re^{-1}\left(\frac{\partial u_t}{\partial s} - \kappa^{(t)} u_n + \frac{\boldsymbol{u}\cdot\hat{\boldsymbol{r}}}{r}\right) + O(\delta^3). \quad (4.18)$$

We assume that the fluid starts off stationary so that all perturbation quantities due to the boundary layer are initially zero. For the case of a bubble bursting we are thus neglecting any vorticity that would have been created in the boundary layer as the bubble rose to the surface.

Certain limiting cases as $r \rightarrow 0$ need to be calculated. By symmetry, u_t, $\partial u_n/\partial s$ and $\partial^2 u_t/\partial s^2$ all vanish on the axis. From this it follows that $\boldsymbol{u}\cdot\hat{\boldsymbol{r}}/r \rightarrow \hat{\boldsymbol{t}}\cdot\nabla\boldsymbol{u}\cdot\hat{\boldsymbol{t}}$ as $r \rightarrow 0$. Also, for motions starting in a perfect state of rest, $A = 0$ on the axis initially, and so (4.5) will ensure that A remains zero there throughout the motion.

Moore (1963) calculated expressions for the boundary layer on a spherical bubble moving through a liquid. He found the boundary-layer approximation to be invalid in a region of width $\delta^{\frac{1}{3}}$ near to the rear of the bubble, owing to separation. Vorticity in this region is confined to a layer of thickness $\delta^{\frac{1}{3}}$, and viscous forces are no longer as important as inertial forces. Closer still to the axis of symmetry, the layer thickens further to form a wake, where stream surfaces are eventually cylindrical and parallel to the axis. The wake region has width $\delta^{\frac{1}{2}}$ so that again diffusive viscous effects are negligible, with the movement of vorticity being dominated by advection. We shall assume that a similar thin wake structure also exists in the case of a non-spherical rising bubble or for a bursting bubble until the jet forms. Jet formation will cause vorticity from a larger region near the underside of the bubble cavity to be advected into the downward jet. From a modelling viewpoint we can correct for this thin wake to a certain extent, provided that the spacing between nodes is not too small, by using an appropriate expression for the perturbation to the normal velocity at the node on the axis beneath the bubble. This normal velocity only directly affects adjacent nodes through the arclength derivatives taken on a cubic spline for A. Indeed, the radial derivative of A which is, apart from a factor of 2, precisely the normal velocity at the end node, is required here in order to fit the cubic spline to A. In order to calculate U_n here, we can use the vertical component of the Navier–Stokes equations. Moore's estimates indicate that inertial terms dominate both viscous and pressure gradient terms, so that we may write

$$\frac{\mathrm{d}}{\mathrm{d}t}\left(\frac{\partial A}{\partial s}\right) = -\frac{\partial A}{\partial s}\frac{\partial^2\phi}{\partial n^2} + \frac{1}{Re}\frac{\partial^2 U_n}{\partial s^2}$$
$$= 2\frac{\partial A}{\partial s}\left(\frac{\partial u_t}{\partial s} - \kappa^{(t)} u_n\right) + \frac{1}{Re}\frac{\partial^2 U_n}{\partial s^2}, \quad (4.19)$$

on using (4.16). The highest-order viscous term is retained in order to start the calculations off, as at the time the boundary-layer calculations commence, all perturbations are assumed zero.

If calculations also include rising bubbles, for a cubic spline to be fitted to A the value of $\partial A/\partial s$ is also required at the top, on the axis of symmetry. Similar to (A 2) in the Appendix, it can be shown that

$$\frac{\partial}{\partial s}\left(\frac{\mathrm{d}A}{\mathrm{d}t}\right)=\frac{\mathrm{d}}{\mathrm{d}t}\left(\frac{\partial A}{\partial s}\right)+\frac{\partial A}{\partial s}\frac{\mathrm{d}\lambda}{\mathrm{d}s}\frac{\mathrm{d}}{\mathrm{d}t}\left(\frac{\mathrm{d}s}{\mathrm{d}\lambda}\right). \tag{4.20}$$

Also, from (A 2)

$$\hat{\boldsymbol{t}}\cdot\nabla\boldsymbol{u}\cdot\hat{\boldsymbol{t}}=\frac{\mathrm{d}\lambda}{\mathrm{d}s}\frac{\mathrm{d}}{\mathrm{d}t}\left(\frac{\mathrm{d}s}{\mathrm{d}\lambda}\right)+O(\delta). \tag{4.21}$$

Combining (4.20), (4.21) and (4.5) and taking the limit as $s\rightarrow 0$, gives an equation for the time evolution of $\partial A/\partial s$ on the axis above a bubble,

$$\frac{\mathrm{d}}{\mathrm{d}t}\left(\frac{\partial A}{\partial s}\right)=-4\left(\frac{\partial u_t}{\partial s}-\kappa^{(t)}u_n\right)\frac{\partial A}{\partial s}+\frac{2}{Re}\left(\frac{\partial^2 u_n}{\partial s^2}+\kappa^{(t)}\frac{\partial u_t}{\partial s}\right)+O(\delta^2). \tag{4.22}$$

The condition on the slope of A at $r=R_{max}$ is found by a consideration of the limiting form of (4.5). Making use of (3.6) and (3.8), we see that $A=O(1/r^4)$ as $r\rightarrow\infty$.

When the walls of the bubble cavity start to move inwards immediately before forming the jet, the vorticity created in the thin boundary layer is advected into the bulk of the liquid. The assumption of a thin boundary layer is violated once this separation takes place, causing the boundary-layer calculations using the method described above to break down. However, we can follow this advection of vorticity from the boundary layer using the vorticity equation,

$$\frac{\mathrm{D}\{\boldsymbol{u}\}\boldsymbol{\omega}}{\mathrm{D}t}\approx\frac{\mathrm{d}\boldsymbol{\omega}}{\mathrm{d}t}=\boldsymbol{\omega}\cdot\nabla\boldsymbol{v}+Re^{-1}\nabla^2\boldsymbol{\omega}. \tag{4.23}$$

Since $\boldsymbol{\omega}=\omega\hat{\boldsymbol{\theta}}$, (4.23) can be written as

$$\frac{\mathrm{D}\{\boldsymbol{u}\}\omega}{\mathrm{D}t}\approx\omega\frac{\boldsymbol{u}\cdot\hat{\boldsymbol{r}}}{r}+Re^{-1}\left(\nabla^2\omega-\frac{\omega}{r^2}\right). \tag{4.24}$$

We assume that the layer is initially thin enough so that derivatives of the pertubation velocity across it are larger than those taken along it, thus the initial vorticity may be approximated by

$$\omega=\frac{\partial U_t}{\partial n}-\frac{\partial U_n}{\partial s}-\kappa^{(t)}U_t\approx\frac{\partial U_t}{\partial n}. \tag{4.25}$$

As the boundary layer separates, viscous terms will become less important, and we may assume that the vorticity development can be described by pure advection together with changes brought about by the stretching of vortex rings moving towards or away from the central axis. Hence by following material points, in the sense defined by the potential flow field, we can calculate an estimate of the vorticity evolution in both the upward and downward jets. We examine *a posteriori* our assumption that the self-induced motion of the vorticity can be neglected when compared to the advection due to the irrotational flow.

4.2. *Repositioning and smoothing*

In order to maintain a good resolution of surfaces, it is necessary to reposition points periodically. Points on bubbles are moved so that they are once again evenly spaced. Points on the free surface are spaced so that the arclengths follow a nonlinear

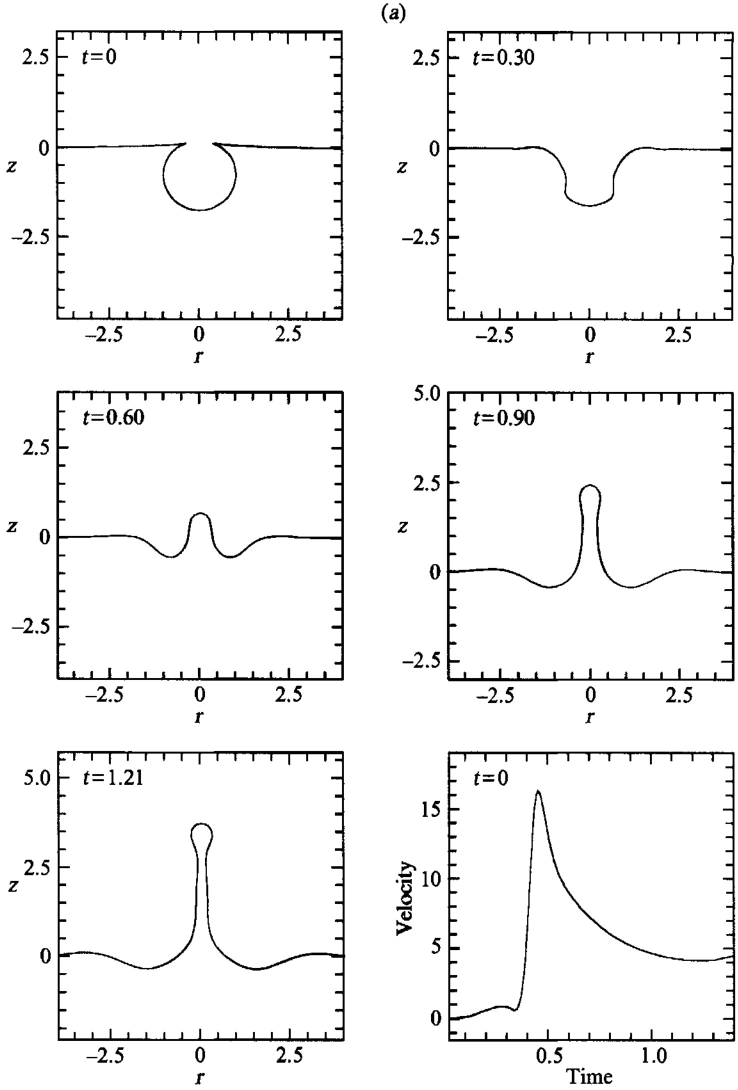

FIGURE 4(*a*). For caption see p. 455.

distribution similar to that in equation (3.5). Regular smoothing of the surface and potentials with the Longuet-Higgins & Cokelet (1976) smoothing formula is also required in order to prevent high-frequency surface oscillations.

As was mentioned in §4.1, finite-difference points in the boundary layer are repositioned with nodes on the surfaces. Since these points must always lie on normals to the surface, this can be done as follows. The standard repositioning of the surface nodes decides between which two old nodes a new node is to be placed. Values of U_t on the new boundary-layer normal are chosen at the same height η as those on the old normal immediately to its left by a simple linear interpolation scheme, based on the assumption that the surface curvature will not change much from one node to the next, so that the three normals meet at a single point. Hence changes in U_t at nodes equidistant from the surface on the normals will be in the same proportion as the arclengths along the surface. To do this the value of U_t on the normal immediately to

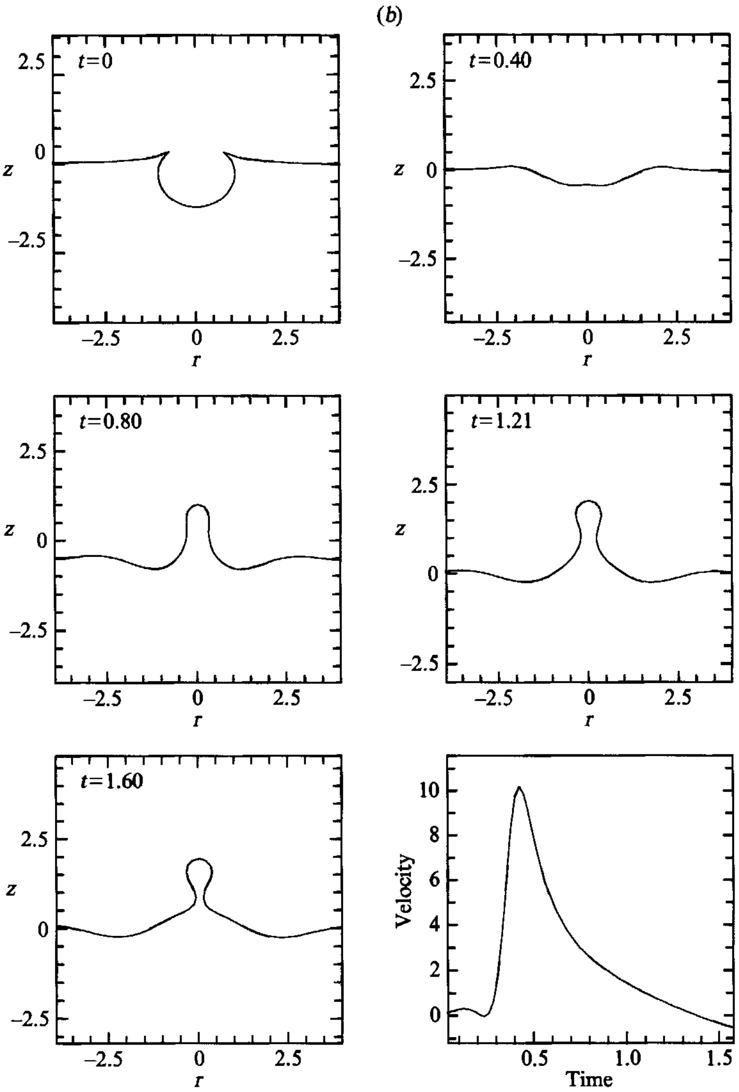

FIGURE 4(*b*). For caption see facing page.

the right of the new normal is also calculated at the same height by quadratic interpolation. This is repeated for all nodes on each normal.

5. Results and discussion

The methods described in the previous sections allow numerical calculation of bubble and interface shapes at various times during bubble rise or burst. A number of interesting cases are shown in figure 4(*a*–*c*) for different bubble sizes. It is clear that smaller bubbles, as their internal pressures are higher, burst from lower in the fluid and thus release a proportionately greater amount of energy in the form of the high-speed liquid jets seen experimentally (see for example Kientzler *et al.* 1954; MacIntyre 1972). The larger bubbles form proportionately wider jets as has been observed in Garner *et al.* (1954). The velocity of the central node on the free surface increases sharply as the jet is formed. In figure 4(*a*, *b*) there is a noticeable drop in velocity immediately before

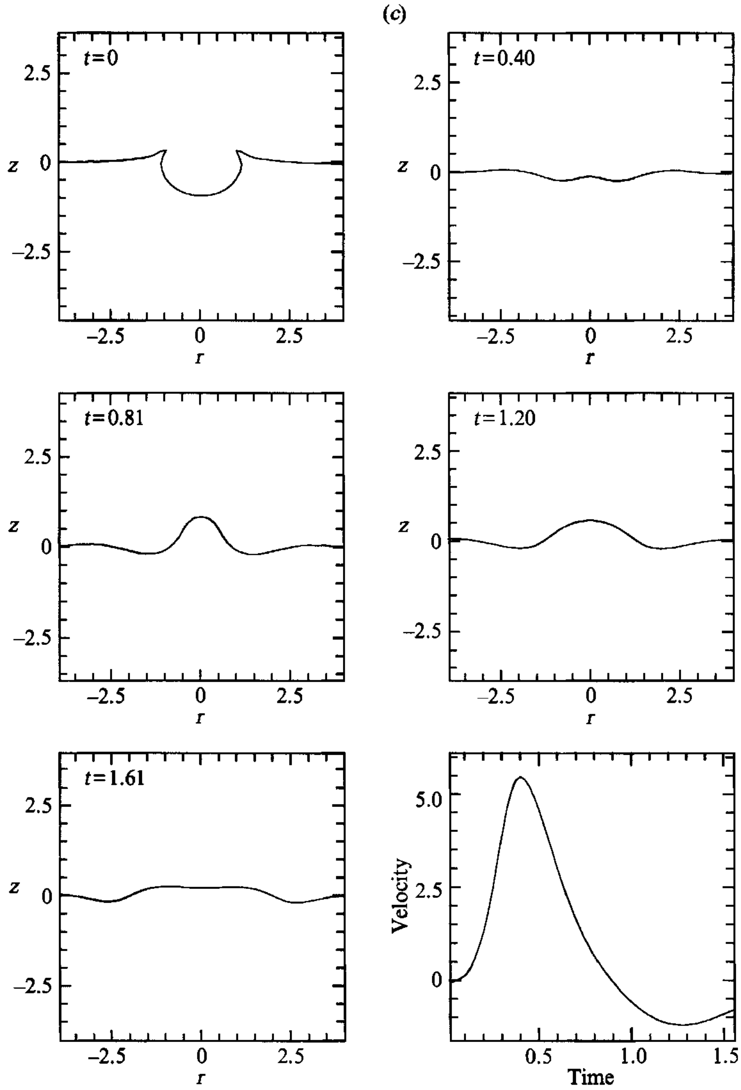

FIGURE 4. Calculated free-surface shapes for different initial bubble sizes, together in each case with the velocity of the node on the central axis. Eötvos numbers are (*a*) 0.30, (*b*) 2.12 and (*c*) 4.77, corresponding to equivalent radii of 0.075, 0.2 and 0.3 cm respectively.

the jet begins to rise. This can be seen more clearly in a magnification of the motion of figure 4(*a*), shown in figure 5. As the cavity walls straighten early on in the burst, the bottom rises slowly and flattens off, creating a ring of high curvature at the 'corner' between the near vertical wall and the horizontal base. The effect of surface tension then pulls this ring inwards. Thus the liquid – which flows from the region of opposite curvature near the highest point of the surface – now flows predominantly towards this ring rather than towards the very lowest part of the cavity. The node on the axis of symmetry is then observed to slow down. As the walls close in further, an axisymmetric cusp almost occurs and the liquid is forced upwards. This high surface curvature and the subsequent large velocities and accelerations suggest possible physical similarities between jet formation and the classes of free-surface flows considered by Longuet-Higgins (1980, 1983).

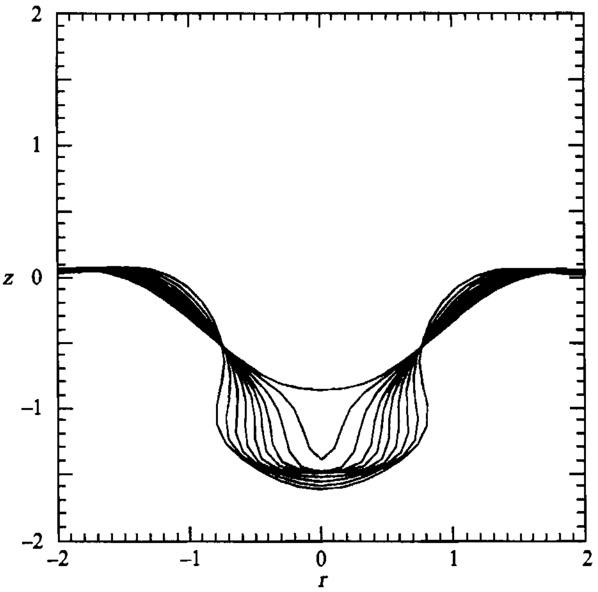

FIGURE 5. A closer look at the motion near to the base of the bubble cavity of figure 4(*a*) as the jet is about to form. The sharpening of the curvature at the corners can be seen as the base becomes flatter. The time between frames is approximately constant.

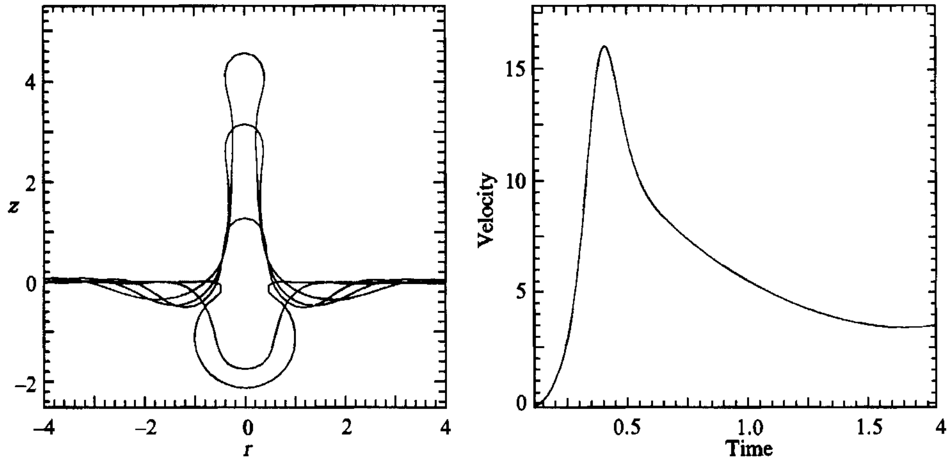

FIGURE 6. A spherical bubble of the same volume as that in figure 4(*c*), burst from a position just below a flat free surface. The bursting motion is not greatly affected by the amount of free surface removed in order to rejoin to the bubble. $Eo = 4.77$, $\gamma_1 = 1.1$, $a = 0.3$ cm.

Bubble equivalent radius (cm)	0.05	0.075†	0.1	0.2†	0.25	0.3†
Jet speed (max) (cm s^{-1})	640	520	410	190	140	94
Drop radius (cm)	0.012	0.017	0.023	0.061	—	—
Drop release time (approx) (ms)	1.8	3.4	5.2	1.4‡	1.5‡	1.7‡

TABLE 1. Dimensional data from calculations

† See figure 4.

‡ Time until maximum jet height.

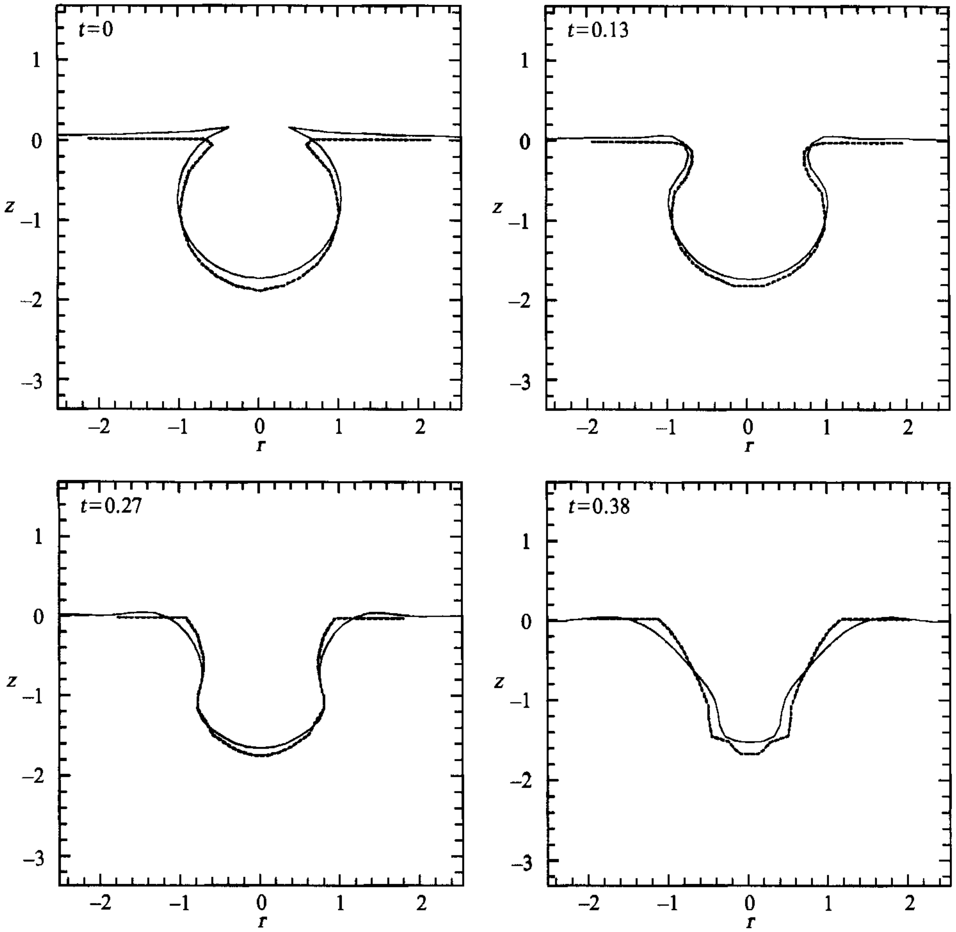

FIGURE 7. Calculated motion of the 0.75 mm bubble (solid lines) compared with the experiments of Kientzler *et al.* (1954) (dashed lines). The exact shapes of the experimental bubble craters near to where they join the free surface are not clear from the photographs in the paper of Kientzler *et al.* (1954) and this may be the cause of some discrepancy. The exposure time for the frames in the photographic study was reckoned by Kientzler *et al.* to be about 65 μs.

The jet accelerates for only a short time, and then slows as it rises. For the smallest bubble, figure 4(*a*), the speed of the uppermost point increases very slightly, once more due to the thinning of the jet and the breaking off of a drop, at which point the calculations must stop. As velocities scale with respect to $(\sigma/\rho a)^{\frac{1}{2}}$, it is clear that smaller bubbles result in faster jets (see table 1).

Compare these calculations with figure 6, where a 3 mm radius bubble is burst from a completely submerged position. Here, unlike in figure 4(*c*), a high-speed jet is formed. Owing to the greater influence of gravity, this jet is wider and not as fast as those produced by smaller bubbles, which burst with similar initial configurations.

The calculated free-surface shapes before jet production are repeated for the 0.75 mm bubble in figure 7 in order to show a comparison with the experimental results of Kientzler *et al.* (1954). Slight differences in the initial motion can be attributed to the fact that the experimental profile starts off slightly lower in the fluid. The jet produced in the experiments, although of speed comparable to that predicted here, is highly asymmetric and breaks up significantly earlier than calculated, so that the comparison

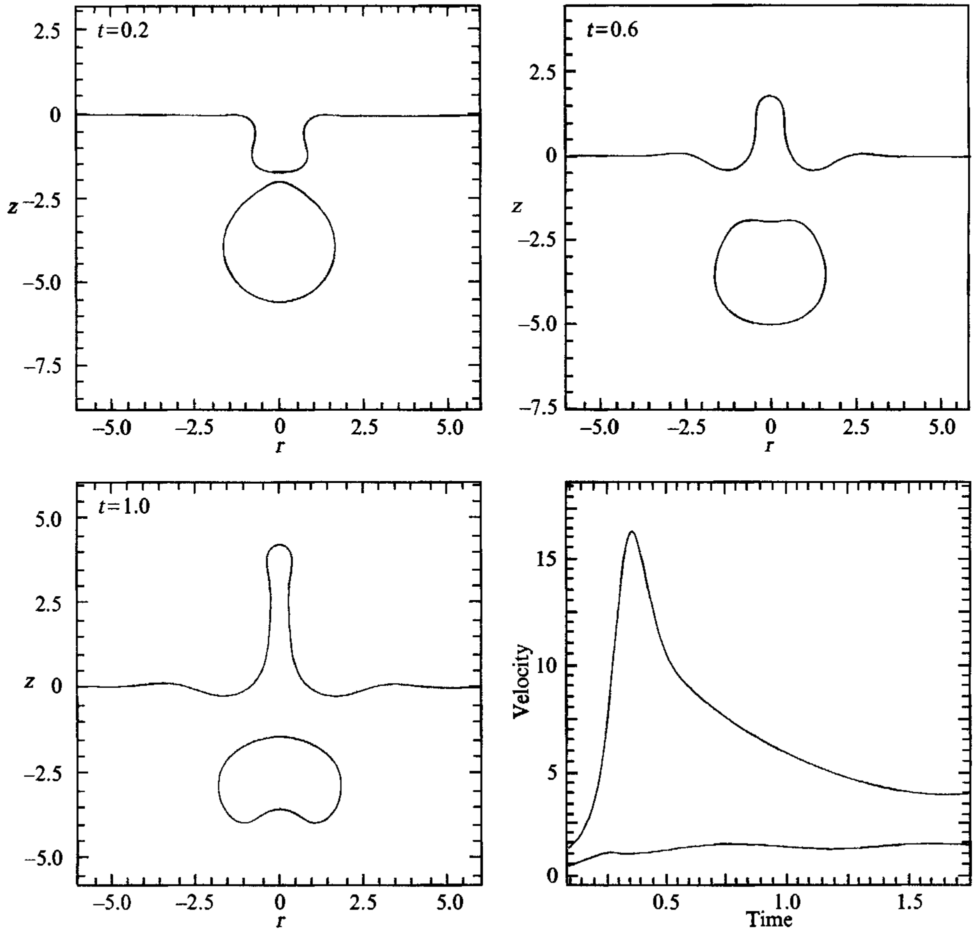

FIGURE 8. The effect of a bursting bubble on a second, larger bubble following close behind, together with a plot of the jet velocity and centroid speed (lower curve) of the lower bubble. $Eo = 4.77$, $\gamma_1 = 1.1$, $\gamma_2 = 4.0$, $a = 0.3$ cm, $r_2 = 1.67$.

for later times is not so good. This is not shown, owing to the difficulty of identifying the surface position of the lower part of the jet which, in the photographs of Kientzler *et al.* (1954), is obscured by the surrounding bubble crater. In addition to the inevitable neglect of asymmetric instabilities, node repositioning and smoothing may cause some discrepancy in the jet shapes. Enhancements to the numerical procedure, to the surface representation or so that smoothing is no longer required, may improve this. The effect of a boundary layer on the jet is discussed below.

The existence of a downward jet in the calculation is confirmed by placing a second bubble directly below the bursting bubble. It can be seen in figure 8 that the top of the second bubble is firstly pulled up by the efect of the low pressure around the highly curved bursting bubble cavity. Then, just as the jet forms, the top of the lower bubble develops a dimple. The lower bubble then begins to rise and soon starts to form a jet from below, characteristic of bubbles of this size. The jet velocity for the bursting bubble reaches a slightly higher peak, but is otherwise largely unaffected by the following bubble. Likewise, the centroid velocity of the following bubble, indicated by the lower trace of the velocity plot for figure 8, undergoes a small dip as the jet of the bursting bubble forms.

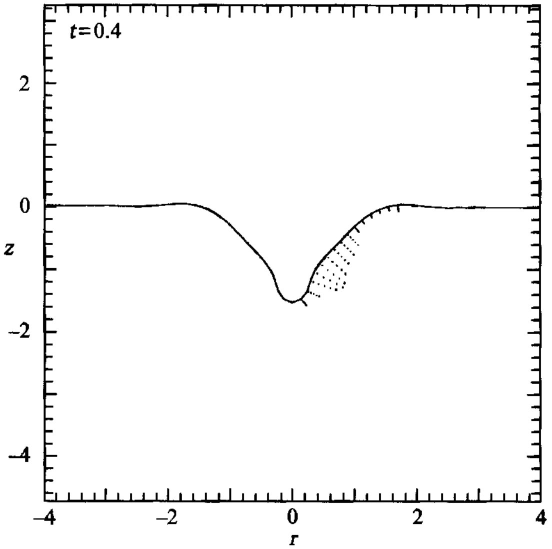

FIGURE 9. Boundary-layer separation before jet formation is indicated by the motion of boundary-layer nodes away from the rapidly retreating surface.

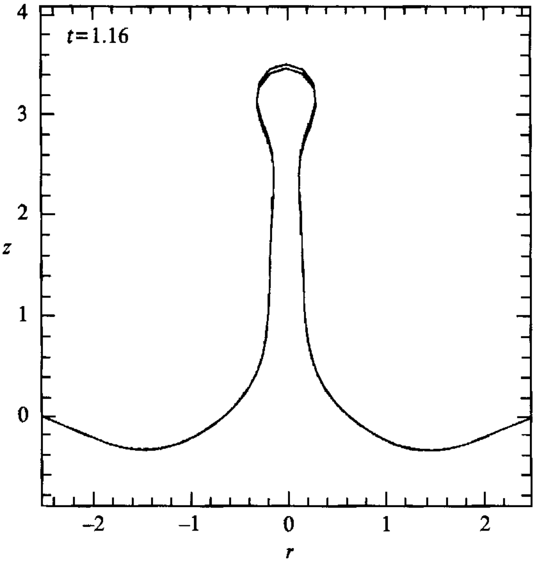

FIGURE 10. Starting the boundary-layer calculations just after the jet forms shows the dissipative effect of viscosity, resulting in a slightly shorter jet compared to the purely potential flow case.

Using the boundary-layer calculations of §4, we find that the surface shapes, up until jet formation, are indistinguishable from those in the figures above. Unfortunately boundary-layer separation over a significant region occurs just before the jet forms (figure 9) so that the boundary-layer calculation must stop. The dissipative effect of viscosity on the jet can be seen by allowing a boundary layer to develop just after the jet has begun to form (at $t = 0.5$ for the 0.75 mm case). Calculations run as far as the time when the droplet at the end of the jet begins to develop. Figure 10 shows the resulting jet to be very slightly shorter than in the corresponding potential flow case at the same time.

The pressure in the fluid is calculated using the Bernoulli formula (2.2) together with the boundary-layer modification (4.7). To improve resolution near to the surface, where the boundary integral formula for the potential in the fluid is badly behaved, the pressure there is given by

$$p^* - p_\infty = \mathrm{d}k_m/\mathrm{d}t + \kappa_m - \kappa + \tfrac{1}{4}\gamma_m Eo + \frac{2}{Re}\hat{\boldsymbol{n}}\cdot\boldsymbol{e}\cdot\hat{\boldsymbol{n}}, \tag{5.1}$$

where $\boldsymbol{e} = e_{ij}$ is the rate-of-strain tensor. Since the fluid is incompressible,

$$\hat{\boldsymbol{n}}\cdot\boldsymbol{e}\cdot\hat{\boldsymbol{n}} = -\frac{\partial u_t}{\partial s} + u_n\kappa^{(t)} - \frac{\boldsymbol{u}\cdot\hat{\boldsymbol{r}}}{r} + O(\delta). \tag{5.2}$$

As cells are more likely to be ripped apart by straining flows than by a strong velocity gradient in one particular direction, when damage can be reduced by the cells rotating with the fluid, the energy dissipation rate, $\Phi = 2\mu e_{ij} e_{ij}$, gives a good indication of the stresses placed on a cell in the fluid, thereby providing a possible measure of the damaging nature of a particular flow field.

In the fluid, outside the boundary layer, the non-zero rates of strain are given by

$$e_{rr} = \frac{\partial u_r}{\partial r}; \quad e_{\theta\theta} = \frac{u_r}{r}; \quad e_{zz} = \frac{\partial u_z}{\partial z}; \quad e_{rz} = \frac{1}{2}\left\{\frac{\partial u_r}{\partial z} + \frac{\partial u_z}{\partial r}\right\}. \tag{5.3}$$

At the surface, by virtue of the stress-free boundary condition, the rates of strain are

$$e_{nn} = -\frac{\partial u_t}{\partial s} + u_n\kappa^{(t)} - \frac{\boldsymbol{u}\cdot\hat{\boldsymbol{r}}}{r} + O(\delta); \quad e_{tt} = \frac{\partial u_t}{\partial s} - \kappa^{(t)}u_n + O(\delta); \quad e_{\theta\theta} = \frac{\boldsymbol{u}\cdot\hat{\boldsymbol{r}}}{r} + O(\delta), \tag{5.4}$$

with all off-diagonal terms zero. By exploiting incompressibility, the corresponding dimensional energy dissipation rate at the surface may be written as

$$\Phi = 4\mu(e_{nn}^2 + e_{tt}^2 + e_{nn}e_{tt}). \tag{5.5}$$

The pressures above atmospheric pressure (dyn cm^{-2}) for the 0.75 mm and 3 mm bubbles are plotted in figures 11(*a*) and 11(*b*) respectively (plate 1). For the smaller bubble, the initial motion is driven by the very high pressure around the rim of the cavity. This is less dramatic in the 3 mm case where gravity also plays a significant role in shaping the motion. In the first two frames of figure 11(*a*), the low pressure around the underside of the bubble intensifies as the wave of fluid that was initially just below the neck of the bubble crater moves down the bubble, increasing in curvature. As the walls of the cavity collapse inwards a ring of high pressure can be seen to develop. This then moves downwards until it finally becomes a point of high pressure directly beneath the bubble (at $t \approx 0.46$). This pushes fluid upward and downward to produce the jets evident in previous figures. The high pressure remains during the early stages of jet formation (final frame of 11*a*), further accelerating fluid into the jet. The pressure in the jet is relatively high owing to surface tension which acts so as to thin it until one or more drops break off. For the large bubble, the pressure rises only slightly as the much smaller jet is about to form. This can be seen through the slight upward bending of the contour lines of the highly visible hydrostatic pressure.

Figure 12 shows that the largest maximum pressures occur for the smallest bubbles.

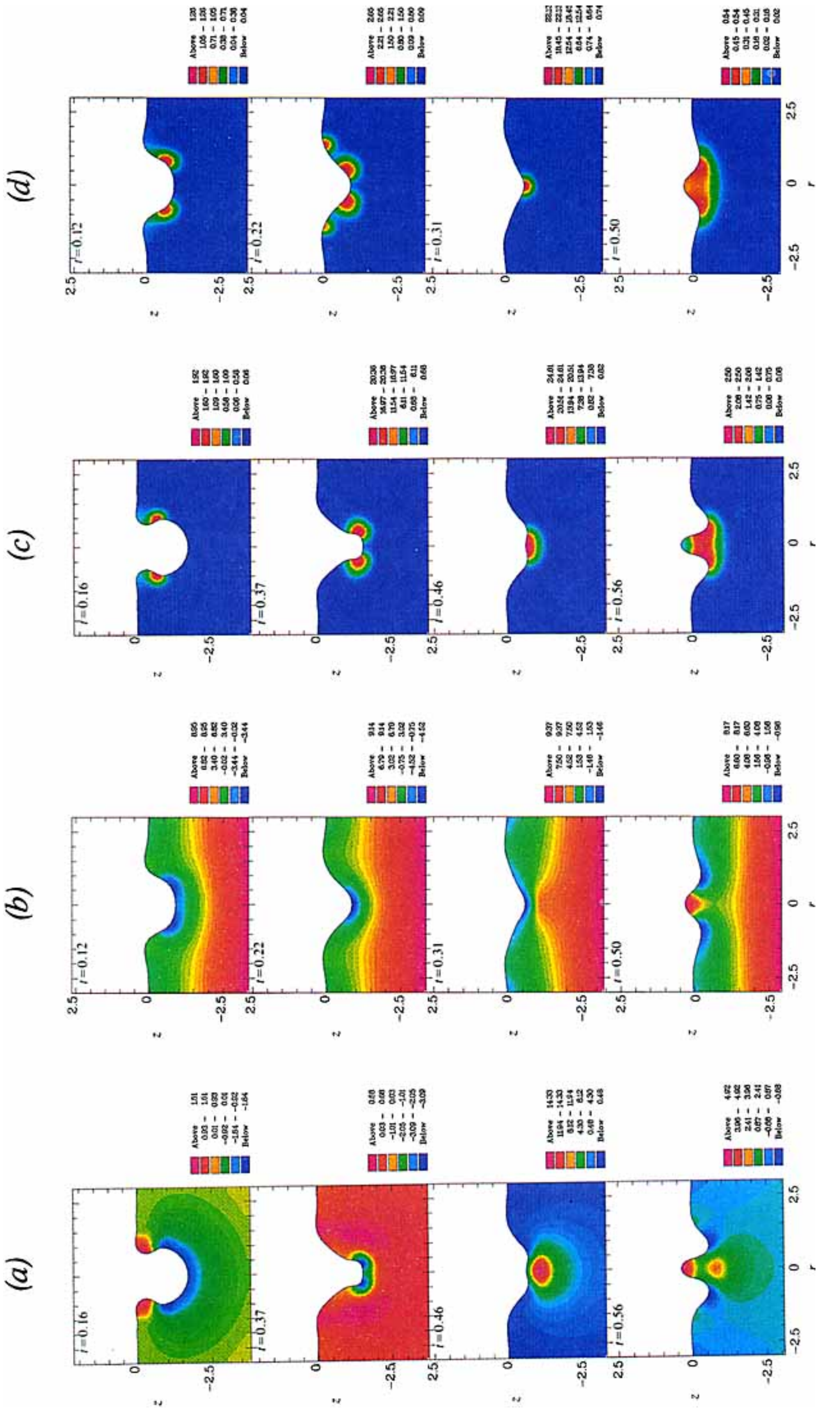

FIGURE 11. *(a, b)* The pressure above ambient pressure (10^3 and 10^2 dyne cm^{-2}) for the 0.75 mm bubble of figure 4*(a)* and the 3 mm bubble of figure 4*(c)*, respectively. *(c, d)* The corresponding energy dissipation rates in units of 10^5 and 10^3 dynes $\mathrm{cm}^{-2}\,\mathrm{s}^{-1}$.

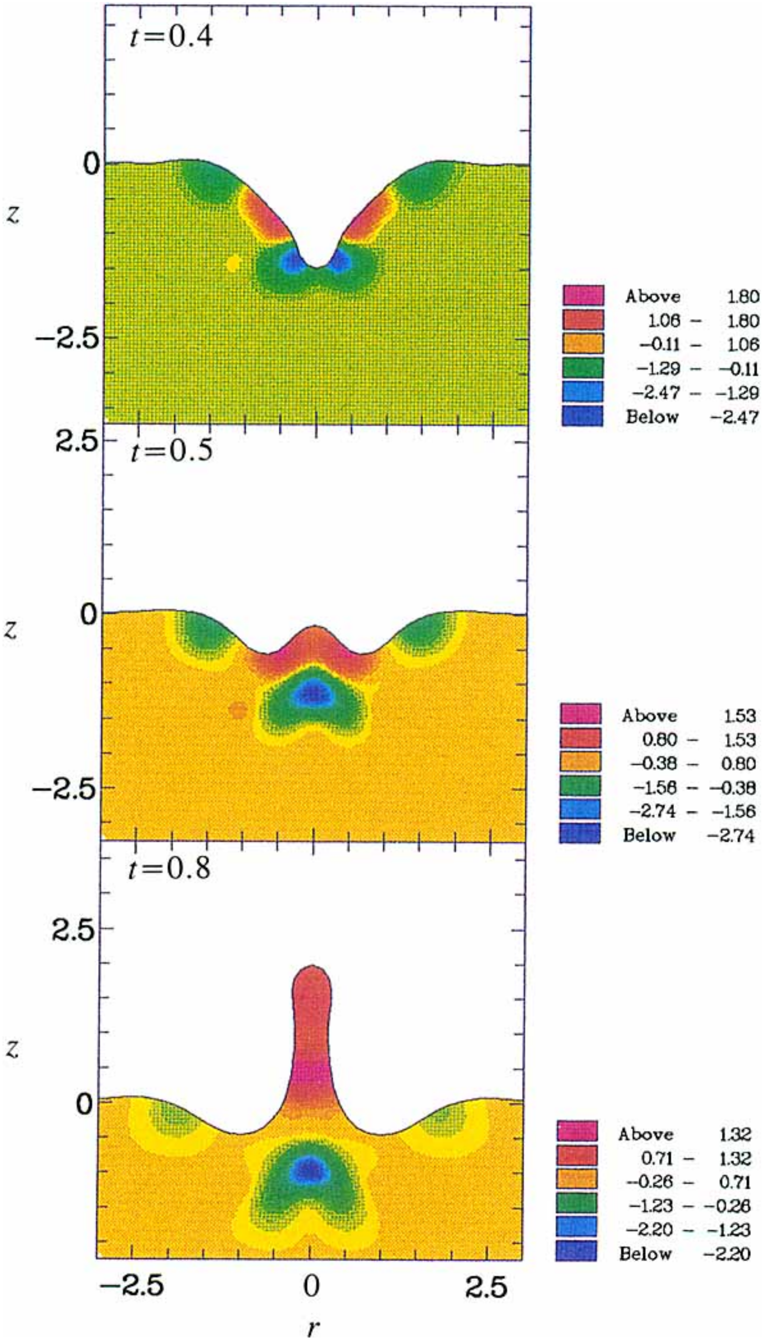

FIGURE 15. The vorticity distribution ($10^2\,s^{-1}$) generated in the boundary layer and subsequently advected into the fluid by the upward and downward jets. The case of the 0.75 mm bubble of figure 4*(a)* is shown here.

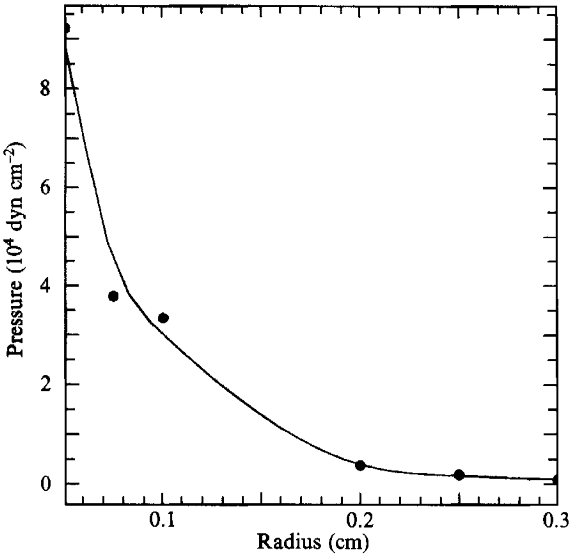

FIGURE 12. Maximum pressures produced throughout the bursting process plotted against bubble radius.

This was expected from the experimental studies on cell damage. However, it seems that the pressures themselves are insufficient to kill cells, being equivalent to only a few centimetres of water.

Figures 11(*c*) and 11(*d*) (plate 1) show the corresponding energy dissipation rates (dyn cm^{-2} s^{-1}) for the same times as above. It is seen that the peak energy dissipation rate moves round with the wave of fluid, where the pressure is low, increasing in magnitude until the jet forms. MacIntyre (1972) indicated that this ripple was a site where high rates of strain were likely. Indeed, high rates of strain are to be expected when the jet is forming owing to the extensional flow around a stagnation point near to the pressure maximum. Fluid must be drawn in from the sides towards the axis of symmetry and then rapidly accelerated upwards or downwards into one of the jets. Such flows are potentially lethal to cells, which may be stretched and ruptured by the high strain rates. Figure 13 shows that the maximum energy dissipation rates, which occur beneath the bubble immediately before jet formation, increase rapidly with decrease in bubble radius. Again, this is in keeping with the finding that cell damage is greater for smaller bubbles. There is no complete agreement on the strength of cells. Orton & Wang (1990) suggest that stresses of the order of 10^3 dyn cm^{-2} are sufficient to cause death, whereas Zhang *et al.* (1991) give cell bursting pressures of about 5×10^4 dyn cm^{-2}. The calculated maximum energy dissipation rates for the smallest bubbles are equivalent to stresses of the order of 10^4 dyn cm^{-2}, indicating that bubble bursting can create an hydrodynamic environment which may be deadly for cells.

The boundary layer makes almost no difference to the calculated values of energy dissipation rate. This is mainly because the effect of the boundary layer in ensuring zero tangential stress at the surface is exploited even when no boundary layer is being used in the calculations, in order to improve resolution in the contouring program.

It was proposed by Orton & Wang (1990) that cell death rates are closely related to the rate of liquid entrainment from bursting bubbles. As it seems reasonable to assume that the underlying cause of cell damage must be some form of hydrodynamic stress, there should be a corresponding relationship between this stress and the entrainment

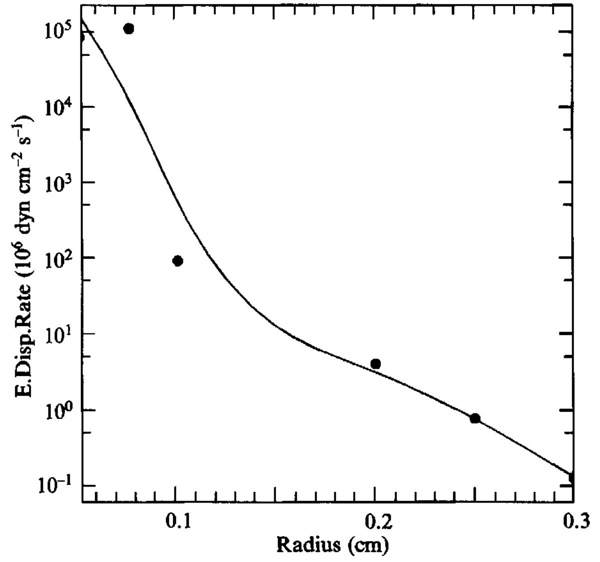

FIGURE 13. Maximum energy dissipation rates produced throughout the bursting process, plotted against bubble radius. The logarithmic scale indicates an exponential dependence of maximum stress on bubble radius for larger bubbles. The slight drop in the data point for the smallest bubble as compared to the next smallest may be because of the difficulty in locating the exact place and time of the peak, due to large spatial and temporal gradients beneath the forming jet.

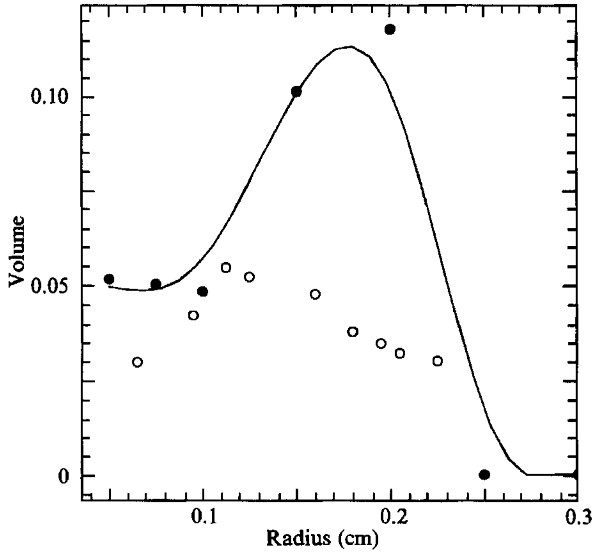

FIGURE 14. Non-dimensional jet drop volumes against bubble radius: calculated (solid circles and line), compared with the experimental values of Garner *et al.* (1954) (open circles).

rate. To investigate this, we calculated estimates for the volume of the first drop released. The calculated entrainment rates are compared with the jet drop sizes of Garner *et al.* (1954) in figure 14. Note that only the size of the first released drop is calculated and no allowance is made for the volume of fluid entrained by the rupture of the film above the bubble, which is significant for only the largest bubbles (see Garner *et al.* 1954). The droplet sizes for the smaller bubbles agree to an order of magnitude. Differences are partly because of the difficulty in predicting the precise time and place of disengagement, but are also due to discrepancies in the jet formation itself pointed out above. Smoothing and repositioning of nodal points in the jets may smooth out small-scale instabilities that would otherwise affect drop formation. An interesting point to note is that the calculated entrainment rates seem to be at a maximum for bubles of radii around 2 mm. Even though the bubble of figure 4(*b*) does not form a long, thin jet, the relative volume of the drop released is much larger than that of the three smallest bubbles studied. When this calculation was allowed to continue past the point where the drop almost disengaged, the code did not break down, but the jet fell back into the fluid. In reality, it would be surely be pinched off by surface tension, before falling back into the fluid. We can therefore conclude that 2 mm must be close to the bubble radius beyond which no drop is released. Garner *et al.* (1954) suggest that this cut-off point for jet drop formation is at about 2.5 mm. The velocity plot of figure 4(*b*) shows that, at the time of droplet formation, the top of the jet is moving slowly downwards. If this is the case, such large droplets near to the cut-off point may not have been identified as such by the experimenters whose methods hinged on observations and detection of drops thrown some distance above the jet. That larger droplets are formed for larger bubbles is noted by Garner *et al.* (1954), but the sizes are still small in comparison with our calculations.

The approximate vorticity distribution (s^{-1}) is shown at three stages of jet formation in figure 15 (plate 2). This vorticity was created in a boundary layer by the initial collapse of the crater for the 0.75 mm bubble and shed prior to jet formation. Here, it is shown being advected into the bulk of the fluid by the formation of the jets. The self-induced velocity of a hollow vortex ring around which there is a circulation Γ is (Hicks 1884)

$$V = \frac{\Gamma}{4\pi R}\left[\log\left(\frac{8R}{b}\right) - \frac{1}{2}\right],$$

where R is the ring radius and b is the core radius. If we assume that the vorticity in a ring is approximately constant so that, ignoring curvature effects of the ring, the vorticity is related to the circulation by $\Gamma = \pi b^2 \omega$. From figure 15, typical parameter values are $\omega = 2\times 10^2\ \mathrm{s}^{-1}$, $b = 2.5\times 10^{-2}$ cm, $r = 5\times 10^{-2}$ cm giving $V \approx 1.5\ \mathrm{cm\,s}^{-1}$. The jet speed is typically of the order of 150 cm s^{-1}, and the speed of the lower blobs of vorticity can be measured to be about 50 cm s^{-1}, thus confirming the assumption that we could ignore the self-induced velocity.

The sign of the vorticity in the first frame of figure 15 can be explained in terms of the dissipative effect of viscosity, which reduces tangential velocity gradients at surfaces to zero. As the vorticity is dominated by $\partial U_t/\partial n$, it will be negative in sign when $\partial u_t/\partial n$ is positive. This was verified by examining the values of $\partial u_t/\partial n$ at time $t = 0.40$. (In fact $\partial u_n/\partial s + \kappa^{(t)} u_t$ was used as it is easier to calculate accurately, owing to the singular nature of the boundary integral formulation. See (A 6).) In this first frame, the sign of the vorticity was observed to be generally opposite to that of the tangential velocity, u_t. Bearing in mind that normals are directed out of the fluid, this implies that at this time the tangential flow speed at the surface is generally faster than nearby in the bulk of the fluid.

It should be emphasized that although the vorticity carried into the jet is positive, large negative curvatures and tangential velocities near the top of the fully developed jet ensure that the tangential speed near to the surface is greater than at the surface. There is consequently a net negative vorticity at the surface due to additional vorticity created in the boundary layer of the jet which is not accounted for in these figures. As the jet begins to form, and in the lower parts of the jet of the final frame, the tangential velocity of the surface is higher so that the direction of fluid rotation as depicted is correct. As a droplet begins to develop, a region of positive curvature is formed. Thus negative surface values of $\partial u_t/\partial n$ and positive vorticities are found in this region. If we move further down the jet, the thinning becomes less noticeable and a further change of the sign of the surface vorticity takes place. More sign changes are observed to occur around the base of the jet.

The magnitude of the vorticity suggests that viscous effects make only a very small contribution to the stresses in the downward jet region.

6. Conclusion

We have developed a numerical model of bursting bubbles from the time immediately after the rupturing of the film until jet and drop formation. The formation of a jet can be seen as the inevitable result of the collapse towards the axis of symmetry of a bubble crater so that fluid is forced upwards. High-speed jets do not feature in large-bubble (over about 2.5 mm radius) bursts where there is insufficient potential energy in the initial configuration.

High energy dissipation rates prior to jet rise have been identified as an indicator of possible cell damage. The maximum values of energy dissipation rates are reduced approximately exponentially as bubble radius is increased. The full implications of this can only become apparent when we know more details of the likely position of cells in relation to regions of high rates of strain, both around the crater as it collapses and below the bubble as the jets form. The survivability of specific flow environments also needs to be studied in more depth before any concrete conclusions are drawn in this respect.

A technique for including viscous forces in a stress-free boundary layer, based on the method of Lundgren & Mansour (1988), is introduced. The only noticeable effect of the boundary layer on the motion is on the jet, which is slowed slightly due to viscous dissipation. The onset of boundary-layer separation gives initial conditions for an estimate of the vorticity development in the upward and downward jets. This suggests only a small contribution to the total stress placed on cells.

The authors are grateful to Dr Adam Kucera and Dr John Best for the use of their code as a basis for this work and to Professor Alvin Nienow, Mr Nick Emery and Dr Colin Thomas of the School of Chemical Engineering at the University of Birmingham. J.M.B.-S. would also like to thank SERC for financial support.

Appendix

We may easily show that a material curve that is locally normal to a stress-free surface will remain so. First, consider a general material curve indexed by the Lagrangian parameter λ. If the unit tangent to the curve is $\hat{\boldsymbol{m}}$ then

$$\hat{\boldsymbol{m}}\cdot\nabla\boldsymbol{v} = \frac{\partial}{\partial s}\left(\frac{\mathrm{d}\boldsymbol{x}}{\mathrm{d}t}\right) = \frac{\mathrm{d}\lambda}{\mathrm{d}s}\frac{\partial}{\partial\lambda}\left(\frac{\mathrm{d}\boldsymbol{x}}{\mathrm{d}t}\right). \tag{A 1}$$

As both derivatives are taken in a Lagrangian sense, they may be interchanged to give

$$\hat{\boldsymbol{m}}\cdot\nabla\boldsymbol{v} = \frac{\mathrm{d}\lambda}{\mathrm{d}s}\frac{\mathrm{d}}{\mathrm{d}t}\left(\frac{\mathrm{d}s}{\mathrm{d}\lambda}\frac{\partial\boldsymbol{x}}{\partial s}\right) = \frac{\mathrm{d}\hat{\boldsymbol{m}}}{\mathrm{d}t} + \hat{\boldsymbol{m}}\frac{\mathrm{d}\lambda}{\mathrm{d}s}\frac{\mathrm{d}}{\mathrm{d}t}\left(\frac{\mathrm{d}s}{\mathrm{d}\lambda}\right). \tag{A 2}$$

Thus if $\hat{m}$ is chosen to be the normal or tangent to the surface, then

$$\hat{n}\cdot\nabla v\cdot\hat{t}=\frac{\mathrm{d}\hat{n}}{\mathrm{d}t}\cdot\hat{t} \quad \text{or} \quad \hat{t}\cdot\nabla v\cdot\hat{n}=\frac{\mathrm{d}\hat{t}}{\mathrm{d}t}\cdot\hat{n}. \tag{A 3}$$

By using (4.2) and adding the equations of (A 3), we see that for a stress-free surface,

$$\frac{\mathrm{d}\hat{n}\cdot\hat{t}}{\mathrm{d}t}=0. \tag{A 4}$$

In order to calculate normal derivatives of the tangential velocity, u_t, we use the fact that $\boldsymbol{u}$ is irrotational to rewrite it in terms of tangential derivatives of the normal velocity, u_n, which can be calculated more accurately. As the tangent vector is fixed with respect to small changes in the normal direction,

$$\frac{\partial u_t}{\partial n}=\hat{n}\cdot\nabla\boldsymbol{u}\cdot\hat{t}. \tag{A 5}$$

Since $\boldsymbol{u}$ is irrotational, the rank-2 tensor $\nabla\boldsymbol{u}$ is symmetric, so that the right-hand side of (A 5) can be reordered, giving

$$\frac{\partial u_t}{\partial n}=\hat{t}\cdot\nabla\boldsymbol{u}\cdot\hat{n}=\frac{\partial u_n}{\partial s}+\kappa^{(t)}u_t. \tag{A 6}$$

REFERENCES

Allan, R. S., Charles, G. E. & Mason, S. G. 1961 The approach of gas bubbles to a gas/liquid interface. *J. Colloid Sci.* **16**, 150–165.

Bavarian, F., Fan, L. S. & Chalmers, J. J. 1991 Microscopic visualization of insect cell–bubble interactions I: Rising bubbles, air-medium interface, and the foam layer. *Biotech. Prog.* **7**, 140–150.

Best, J. P. & Kucera, A. 1992 A numerical investigation of non-spherical rebounding bubbles. *J. Fluid Mech.* **245**, 137–154.

Bikerman, J. J. 1973 *Foams.* Springer.

Blanchard, D, C. & Syzdek, L. D. 1972 Concentration of bacteria in jet drops from bursting bubbles. *J. Geophys. Res.* **77**, 5087–5099.

Boris, J. P. 1989 New directions in computational fluid dynamics. *Ann. Rev. Fluid Mech.* **21**, 345–385.

Chalmers, J. J. & Bavarian, F. 1991 Microscopic visualization of insect cell–bubble interactions II: The film and bubble rupture. *Biotech. Prog.* **7**, 151–159.

Clift, R., Grace, J. R. & Weber, M. E. 1978 *Bubbles, Drops, and Particles.* Academic.

Culick, F. E. C. 1960 Comments on a ruptured soap film. *J. Appl. Phys.* **31** (I), 1128–1129.

Garner, F. H., Ellis, S. R. M. & Lacey, J. A. 1954 The size distribution and entrainment of droplets. *Trans. Instn Chem. Engrs* **32**, 222–235.

Guerri, L., Lucca, G. & Prosperetti, A. 1981 A numerical method for the dynamics of non-spherical cavitation bubbles. *Proc. 2nd Intl Colloq. on drops and bubbles, California JPL Publication* 82–7, pp. 175–181.

Hahn, P.-S., Chen, J.-D. & Slattery, J. C. 1985 Effects of London–van der Waals forces on the thinning and rupture of a dimpled liquid film as a small drop or bubble approaches a fluid–fluid interface. *AIChE J.* **31**, 2026–2038.

Handa, A. 1986 Gas–liquid interfacial effects on the growth of hybridomas and other suspended mammalian cells. PhD. thesis, University of Birmingham, UK.

Handa, A., Emery, A. N. & Spier, R. E. 1987 On the evaluation of gas–liquid interfacial effects on hybridoma viability in bubble column bioreactors. *Dev. Biol. Stand.* **66**, 241–253.

HICKS, W. M. 1884 On the steady motion and small vibrations of a hollow vortex. *Phil. Trans. R. Soc. Lond.* A **175**, 183.

IVANOV, B. I., KRALCHEVSKY, P. A. & NIKOLOV, A. D. 1986 Film and line tension effects on the attachment of particles to an interface. Parts I–IV. *J. Colloid Interface Sci.* **102**, 97–143.

KIENTZLER, C. F., ARONS, A. B., BLANCHARD, D. C. & WOODCOCK, A. H. 1954 Photographic investigation of the projection of droplets by bubbles bursting at a water surface. *Tellus* **6**, 1–7.

KIOUKIA, N. 1990 Physical and chemical factors affecting hybridoma growth. MSc dissertation, University of Birmingham, UK.

KIRKPATRICK, R. D. & LOCKETT, M. J. 1974 The influence of approach velocity on bubble coalescence. *Chem. Engng Sci.* **29**, 2363–2373.

KUNAS, K. T. & PAPOUTSAKIS, E. T. 1990 Damage mechanisms of suspended animal cells in agitated bioreactors with and without bubble entrainment. *Biotech. Bioengng* **36**, 476–483.

LEVICH, V. G. 1962 *Physicochemical Hydrodynamics.* Prentice-Hall.

LO, L. L. 1983 The meniscus on a needle – a lesson in matching. *J. Fluid Mech.* **132**, 85–78.

LONGUET-HIGGINS, M. S. 1980 On the forming of sharp corners at a free surface. *Proc. R. Soc. Lond.* A **371**, 453–478.

LONGUET-HIGGINS, M. S. 1983 Bubbles, breaking waves and hyperbolic jets at a free surface. *J. Fluid Mech.* **127**, 103–121.

LONGUET-HIGGINS, M. S. & COKELET, E. D. 1976 The deformation of steep surface waves on water. I. A numerical method of computation. *Proc R. Soc. Lond.* A **350**, 1–26.

LUNDGREN, T. S. & MANSOUR, N. N. 1988 Oscillations of drops in zero gravity with weak viscous effects. *J. Fluid Mech.* **194**, 479–510 (referred to herein as LM).

LUNDGREN, T. S. & MANSOUR, N. N. 1991 Vortex ring bubbles. *J. Fluid Mech.* **224**, 177–196.

MACINTYRE, F. 1972 Flow patterns in breaking bubbles. *J. Geophys. Res.* **77**, 5211–5228.

MIKSIS, M., VANDEN-BROECK, J.-M. & KELLER, J. B. 1982 Rising bubbles. *J. Fluid Mech.* **123**, 31–41.

MOORE, D. W. 1963 The boundary layer on a spherical gas bubble. *J. Fluid Mech.* **16**, 161–176.

NEWITT, D. M., DOMBROWSKI, N. & KNELMAN, F. H. 1954 Liquid entrainment 1. The mechanism of drop formation from gas or vapour bubbles. *Trans. Instn Chem. Engrs* **32**, 244–261.

OGUZ, H. N. & PROSPERETTI, A. 1989 Surface tension effects in the contact of liquid surfaces. *J. Fluid Mech.* **203**, 149–171.

OH, S. K. W., NIENOW, A. W., AL-RUBEAI, M. & EMERY, A. N. 1989 The effects of agitation intensity with and without continuous sparging on the growth and antibody production of hybridoma cells. *J. Biotechnol.* **1**, 45–62.

OH, S. K. W., NIENOW, A. W., AL-RUBEAI, M. & EMERY, A. N. 1992 Further studies of the culture of mouse hybridomas in an agitated bioreactor with and without continuous sparging. *J. Biotechnol.* **22**, 245–270.

ORTON, D. R. & WANG, D. I. C. 1990 Effects of gas interfaces on animal cells in bubble aerated bioreactors. Paper No. 103B presented at AIChE Annual Meeting, Chicago.

PRINCEN, H. M. 1963 Shape of a fluid drop at a liquid–liquid interface. *J. Colloid Sci.* **18**, 178–195.

RALEIGH, LORD 1891 Some applications of photography. *Nature* **44**, 249–254.

SCHELUDKO, A. 1962 Certain particulars of foam layers. II. Kinetic stability, critical thickness and equilibrium thickness. *Proc. K. Ned. Akad. Wetensch.* B **65**, 87–96.

TAIB, B. B. 1985 Boundary element method applied to cavitation bubble dynamics. PhD. thesis, University of Wollongong, Australia.

TAYLOR, G. I. & MICHAEL, D. H. 1973 On making holes in a sheet of fluid. *J. Fluid Mech.* **58**, 625–639.

VRIJ, A. 1966 Possible mechanism for the spontaneous rupture of thin, free liquid films. *Disc. Faraday Soc.* **42**, 23–33.

ZHANG, Z., FERENCZI, M. A., LUSH, A. C. & THOMAS, C. R. 1991 A novel micromanipulation technique for measuring the bursting strength of single mammalian cells. *Appl. Microbiol. Biotechnol.* **36**, 208–210.